Journal of Inorganic and Organometallic Polymers and Materials (2026) 36:1050–1071
https://doi.org/10.1007/s10904-025-03969-0

RESEARCH

Numerical Modeling and Machine Learning-Assisted Analysis of Ultra-Thin $CuSbS_2$ Solar Cells Incorporating SnS_2 ETL and V_2O_5 BSF Layers

Md. Abdul Monnaf[1] · Avijit Ghosh[1] · Asadul Islam Shimul[2] · Qaium Hossain[3] · Laboni Ferdoush[3] · Mohammad Fokhrul Islam Buian[4] · Anup Kumar Roy[5] · Shahan Ahmed[6] · Md Mahfuzur Rahman[7] · Nondon Lal Dey[8] · Aijaz Rasool Chaudhry[9] · Md Al Imran[5]

Received: 29 April 2025 / Accepted: 20 July 2025 / Published online: 11 August 2025

Abstract

The clean and environmentally friendly characteristics of photovoltaic solar panel research have long been a source of fascination. A promising option for solar absorber material for ultrathin film solar cells is the triple chalcostibite $CuSbS_2$ (Copper Antimony Sulfide) system, It has earth-abundant components, affordable prices, vacuum-free production techniques, and an exceptionally high light absorption coefficient. However, the efficiency of a typical $CuSbS_2$/CdS heterojunction solar panel is extremely low because of the Schottky barrier that forms at the back contact and the significant recombination of carriers at the CdS/$CuSbS_2$ interface. In this article, SnS_2 (tin disulfide) is suggested as a substitute for the CdS layer in $CuSbS_2$-based TFSCs (Thin Film Solar Cells). SnS_2, $CuSbS_2$, and V_2O_5 have been used as ETL (Electron Transport Layer), absorber layer, and BSF (Back Surface Field) layer, respectively. A new n-p-p+heterojunction solar cell based on Al/FTO/SnS_2/$CuSbS_2$/Ni has been designed and simulated using the SCAPS-1D photovoltaic cell simulator. It has been investigated how integrating the V_2O_5 BSF layer affects the photovoltaic performances of the $CuSbS_2$-based heterojunction solar cell, about the back-contact recombination of carriers, and the built-in potential. Furthermore, a systematic study has examined the effects of several device characteristics, including operating temperature, shunt and series resistances, back-contact metalwork function, carrier concentration, and layer thickness. The outcomes are examined in connection with the device's photovoltaic characteristics to maximize the suggested solar cell's efficiency. At high temperatures, the improved $CuSbS_2$-based solar cell exhibits good performance stability and a maximum efficiency of 31.09%, V_{OC} = 1.39 V, J_{SC} = 25.09 mA/cm^2, FF = 88.54%. Additionally, a Random Forest Machine Learning algorithm predicts the optimum PCE (Power Conversion Efficiency) using semiconductor parameters. The model quantifies each parameter's importance using SHAP (Shapley Additive Explanations) values, revealing their contributions. The model predicts performance accurately and provides precise results with a mean correlation coefficient (R^2) of 0.84. This study highlights $CuSbS_2$-based potential as a viable material for sustainable solar cells.

Keywords $CuSbS_2$ · SCAPS-1D · Thin film · Simulation · Efficiency · Machine learning

✉ Avijit Ghosh
avijitghosheee@gmail.com

[1] Department of Electrical and Electronic Engineering, Begum Rokeya University, Rangpur 5400, Bangladesh

[2] Department of Electrical and Electronic Engineering, Gopalganj Science and Technology University, Gopalganj 8100, Bangladesh

[3] Master's of Science in Management of Information Systems, Lamar University, Beaumont, TX 77705, USA

[4] Department of Mechanical Engineering, Lamar University, Beaumont, TX, USA

[5] Phillip M. Drayer Department of Electrical and Computer Engineering, Lamar University, Beaumont, TX, USA

[6] Master of Arts in Social Research & Data Analysis, Montclair State University, Montclair, NJ, USA

[7] Department of Electrical and Electronic Engineering, Uttara University, Holding 77 Beribadh Road, Dhaka 1230, Bangladesh

[8] Department of Physics, University of Louisiana at Lafayette, 104 E University Ave, Lafayette, LA 70504, USA

[9] Department of Physics, College of Science, University of Bisha, P.O. Box 551, 61922 Bisha, Saudi Arabia

1 Introduction

The world's energy consumption is predicted to exceed terawatts (TW) by 2050; hence, widespread adoption of environmentally friendly renewable energy sources is crucial. One renewable energy source that can supply the world's energy needs at the TW level while still having a significant quantity of solar energy left over is solar energy [1]. One potentially effective way to use solar energy is to directly turn it into electrical energy using photovoltaic (PV) devices. The solar panel has been getting better every day since it was first invented. The original generation of solar photovoltaic devices based on crystalline silicon (c-Si) has led the market. It holds around 95% of the worldwide photovoltaic market share, compared to about 5% for the other thin film PV technologies, such as Cu(In, Ga)Se_2 (CIGS), CdTe (Cadmium Telluride), and Si thin film [2]. However, the present limitations of c-Si innovation and c-Si solar cells include thick and expensive Si wafers, high manufacturing temperatures, high vacuum production methods, and other complicated and expensive processing technologies. Many researchers have studied and created new low-cost, earth-abundant thin-film materials and gadget fabrication techniques over the past 50 years to create more affordable, environmentally friendly solar cells [3]. A small number of TFSC technologies, including CIGS (Copper Indium Gallium Selenide), perovskite solar cells (PSC), and CdTe, have received significant attention due to Their Effectiveness surpassing commercial boundaries at this time. Although both CdTe and CIGS technology have made significant strides, the commercial scalability of the previously mentioned solar cells is limited by incorporating material or resource limitations, toxic and earth-rare elements in CdTe solar panel cells, and the challenging manufacturing process of CIGS technology [2, 4] and Consequently, these materials must be substituted with upcoming sustainable energy technology [5]. To get over the material constraints in CIGS and CdTe technology, kesterite structures like $Cu_2ZnSn(S/Se)_4$ with their non-toxic, inexpensive, and earth-abundant components have been thoroughly studied as PV absorbers during the past ten years. At the laboratory level, CZTS (Copper Zinc Tin Sulfide) solar cells now have a record practical efficiency of 13.00% [6]. By October 2024, PSCs were positioned as serious competitors to well-established technologies like as crystalline silicon (c-Si) solar cells, with single-junction PSCs surpassing 26% efficiency, perovskite-silicon tandem cells surpassing 34%, and all-perovskite TSCs (Thin-film Solar Cells) reaching 29% [7]. In accordance with this, the researchers have created CdTe-based TFSCs and CIGS, which are more affordable than traditional TFSCs with PCE exceeding 20% [3]. The high density of defects and significant potential fluctuations at the energy band boundaries cause the huge V_{OC} shortfall ($Eg/q–V_{OC}$) in CZTS/CZTSe devices since CZTS is a defect-prone system. It follows that additional study and development of PV absorber substances are required to identify low-cost, non-toxic, less faulty, readily controlled stoichiometry, chemically stable, and earth-abundant materials for effective TFSCs.

The photovoltaic community has been considering ternary copper-antimony-sulfide and copper-bismuth-sulfide (CAS and CBS, respectively) systems as substitute active layer materials for TFSCs because of their low cost, non-toxicity, and plentiful components [8–13]. Dufton et al.'s 2012 theoretical investigation of $CuSbS_2$ thin films revealed that these films might be used as absorber components for TFSCs in the future [14]. Kumar and Persson anticipated an extremely high absorption coefficient of $CuSbS_2$ very thin films in the visible and infrared areas in 2013, confirming Dufton's main discovery. A p-like Sb state that was confined near the edge of the conduction band was the source of this [15]. The copper-antimony sulfide system comprises four major phases: Cu_3SbS_4 (famatinite), $CuSbS_2$ (chalcostibite), Cu_3SbS_3 (skinnerite), and $Cu_{12}Sb_4S_{13}$ (tetrahedrite). The crystal structure determines the energy band gap between these phases. $Cu_{12}Sb_4S_{13}$ and Cu_3SbS_4, two of these phases, are being researched as thermoelectric materials due to their poor heat conductivity [16, 17]. Thin films of the less studied I-V-VI_2 chalcogenides ($CuSbS_2$) have fundamental optoelectronic characteristics, such as a nearly perfect direct band gap between 1.38 and 1.58 eV. The wide spectrum exhibits a moderate receiver concentration (10^{15}–10^{18} cm^{-3}) and a strong optical absorption ($\alpha = 10^5$ cm^{-1}). This new solar absorber compound seems promising for PV applications due to its low point of melting point (551 °C) and chemically stable phase [18–21]. Growth methods are crucial to the development of inexpensive and easily scalable PV absorber layers in terms of manufacturing costs. There are numerous physical and chemical synthesis methods for creating $CuSbS_2$-based thin films, including CBD (chemical bath deposition), pyrolysis by spray, heating glass/Sb_2S_3/Cu layer under low vacuum conditions, hybrid ink method, deposited by electrolysis Sb-Cu alloys over sulfur, co-evaporation of Sb, Cu, and S pure substances, the low-temperature ALD (atomic layer deposition), and low-cost spin coating method [22–27]. $CuSbS_2$ thin films are therefore becoming more and more popular as a possible active layer material for TFSCs because of their comparatively low synthesis cost compared to other TFSC technologies, non-toxicity of all elements, and Sb, which is more plentiful and less expensive than indium and gallium. Additionally, compared to the CZT(S/Se) system, theoretical investigations of $CuSbS_2$ thin films show that low-energy imperfections are situated far from the band difference center. This

causes $CuSbS_2$ thin films to have a low percentage of bulk centers of recombination [28].

While several studies on the optical, electrical, and structural characteristics of $CuSbS_2$-based thin films have highlighted their promise as a photovoltaic absorber, very few have shown how they might be used in photovoltaic devices [29]. Following the publication of the first $CuSbS_2$ solar panels in 2005, which used the chemical immersion deposition process and had an open circuit voltage of 345 mV and an extremely low short circuit current of 0.2 mA/cm^2, other methods have been used to create $CuSbS_2$-based solar cells [30]. But up till now, every $CuSbS_2$ absorber-based solar panel that has been shown has struggled with extremely low PCE, which is much less than 2% [30–34]. With a V_{OC} of just 470 mV, Banu et al. (2016) exhibited $CuSbS_2$-based solar cells employing a hybrid ink method and obtained the greatest power conversion efficiency of 3.22% [24]. It is well recognized that the main factors limiting the photovoltaic performance of $CuSbS_2$-based solar panels are the absorber layer defects, the dominant interfacial coupling of minority transporters, and undesirable heterojunction topologies [35]. Furthermore, the short dispersion length of carriers in $CuSbS_2$ thin films limits the amount of effective photo-generated separation of carriers, which leads to a low J_{SC} [31].

Due to the direct inheritance of the $CuSbS_2$-based device structure from its CIGS counterpart, currently, available $CuSbS_2$-based solar panels use CdS as the p-n junction partner. However, the CdS/$CuSbS_2$ contact forms a "cliff-like" CBO, which is outside the advantageous 0–0.40 eV "spike-like" CBO (conduction band offset) range [36, 37]. As a result, $CuSbS_2$-based devices have a low V_{OC}. Thus, further research is required to align the energy range at the ETL/$CuSbS_2$ interface and decrease minority carrier recombination to increase the effectiveness of $CuSbS_2$-based photovoltaic systems [36]. Metal oxides are commonly used as ETL in TFSCs. SnS_2, a semiconductor of the n-type with an extremely high electron affinity and a broadband gap (Eg 2.24 eV), has been successfully used in dye-sensitized solar cells and perovskites. As a result, it exhibits potential as an ETL layer for producing solar cells with good performance [38, 39].

In this study, we show that employing V_2O_5 thin films as the BSF layer and SnS_2 thin films as the ETL to create a heterojunction on both sides of the $CuSbS_2$ absorber layer significantly improves V_{OC}, J_{SC}, and therefore PCE in $CuSbS_2$-based solar panels. Generally speaking, direct band gap thin film materials with low electron affinity and high carrier density and mobility are preferred for the BSF (Back Surface Field) layer in solar panels. The p-type semiconductor V_2O_5 is a thermally stable ternary delafossite. It may be used as the BSF layer for the $CuSbS_2$-based solar panel because of its low resistivity, configurable acceptor concentration, programmable band gap between 2.5 and 3.5 eV, and comparatively low electron affinity when compared to the $CuSbS_2$-absorber layer [40]. To our knowledge, this is the first time that we have designed and simulated heterojunction solar cells based on $CuSbS_2$ using the new device structure: Al/FTO/SnS_2/$CuSbS_2$/Ni. Researchers have looked at how the physical characteristics of various layers affect the newly built device's photovoltaic performance.

Recently, both business and academics have become interested in ML (Machine Learning) because of its capacity to do virtual screening considerably more quickly than quantum mechanical calculations. Furthermore, ML algorithms can react instantaneously by taking into account a vast number of datasets, something that humans cannot do [41]. Researchers may save time and money by focusing their search for the best materials by using ML models to predict material attributes and performance [42]. The ML approach can save energy and money by analyzing vast amounts of composition data and establishing an appropriate compositional window [42]. Analyzing and mapping the connections between materials' non-linear physical, chemical, and optoelectronic characteristics and the output data that goes along with them is the basic concept underlying the machine learning technique [43]. The use of various machine learning methods and the identification of an appropriate model that provides the primary regulating elements (device manufacturing stage) are the driving forces behind this effort.

2 Device Construction and Simulation Techniques

2.1 Architecture of the Device

The wafer-based silicon photovoltaic sector is increasingly embracing computerized design and simulation. Commonly used simulation tools for designing and assessing silicon photovoltaic devices include ATLAS, AFORS-HET, PC1D, and Sentaurus TCAD [44–46]. Due to the complex structure & quantum-mechanical characteristics of thin-film systems, the development of thin-film Photovoltaic simulation tools is progressing more slowly than that of wafer-based quartz simulation tools. As of right now, the photovoltaic community may freely access the majority of TFSC simulation programs that are built on 1D. They include AMPS-1D, SCPAS-1D, wxAMPS, and other popular thin-film photovoltaic modeling applications [47–49].

Burgelman states that the perfect thin-film solar cell simulator should have the ability to handle graded materials, support several layers, describe potential discontinuities

in the band of energy at the boundary between layers, and more [48]. We looked through common simulation software programs by the specifications listed in the Refs [48]. to choose the best package for simulating $CuSbS_2$-based solar panels. Because SCAPS-1D satisfies every condition for 1D devices stated in the Refs [48]., It was chosen. The most comprehensive collection of simulation outputs, such as band diagrams of energy, J-V, Q-E, C-f, and C-V, is also provided by it. To calculate the electrical characteristics of PV devices, the SCAPS-1D simulation tool uses sets of PDD (Poisson Drift Diffusion) equations. Three coupled equations are used in the PDD model: carrier transport, the Poisson, and continuity equations of free holes and electrons. SCAPS-1D numerically calculates the electrical characteristics of Photovoltaic devices by solving these three coupled simultaneous differential equations with suitable boundary conditions in one dimension and steady state. The suggested TFSC structure and band diagram, both with and without BSF, are displayed in Fig. 1a–d using the SCAPS-1D simulating program. The photovoltaic cell's structure was as follows: Fig. 1 shows the Al/FTO/SnS_2/$CuSbS_2$/V_2O_5/Ni, with neutral defect layers at the V_2O_5/$CuSbS_2$ and $CuSbS_2$/SnS_2 interfaces.

We Know,

$$\mathrm{CBO} = \chi_{\mathrm{Absorber}} - \chi_{(\mathrm{HTL})} \tag{1}$$

$$\mathrm{VBO} = \chi_{(\mathrm{HTL})} - \chi_{\mathrm{Absorber}} + \mathrm{Eg}_{(\mathrm{HTL})} - \mathrm{Eg}_{(\mathrm{Absorber})} \tag{2}$$

Where,

CBO = Conduction band offsets.
VBO = Valance band offsets.
X = Electron affinity.
E_g = Energy band gap.

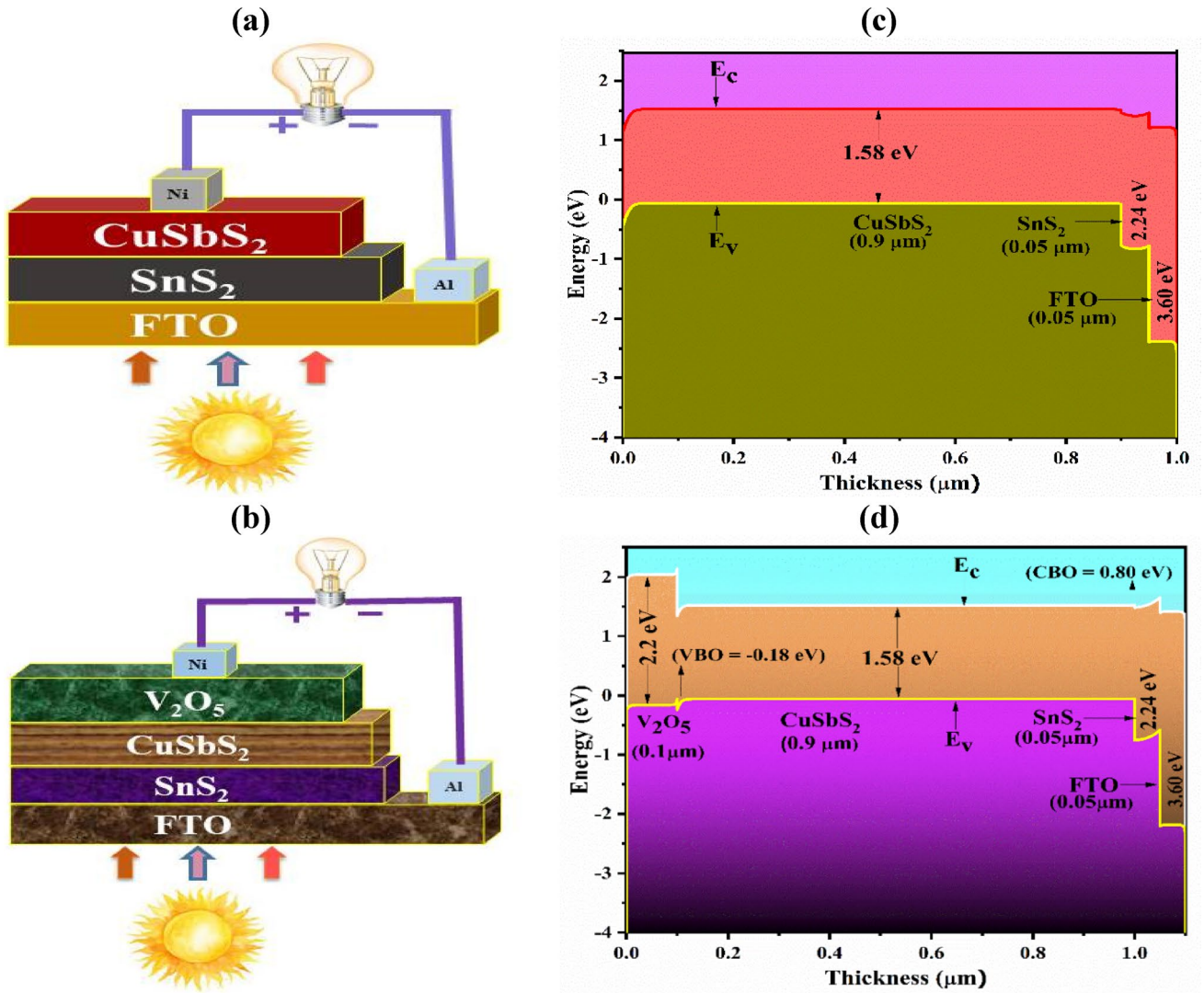

Fig. 1 Al/FTO/SnS_2/$CuSbS_2$/Ni heterojunction solar cells without and with BSF are shown schematically in (**a**, **c**), and energy band diagrams in (**b**, **d**), respectively

Table 1 The SCAPS-1D simulation's absorber setups, FTO, ETL and BSF are summarized

Parameter (unit)	FTO [52]	SnS_2 [52]	$CuSbS_2$ [2]	V_2O_5 [53]
Thickness (μm)	0.05	0.05	0.90	0.10
Bandgap (eV)	3.60	2.24	1.58	2.20
Electron affinity (eV)	4.50	4.24	4.20	3.40
Permittivity of dielectrics (relative)	10	10	14.60	8.00
CB density of effective states (cm^{-3})	2.00×10^{18}	2.20×10^{18}	2.0×10^{18}	9.2×10^{19}
VB density of effective states (cm^{-3})	1.80×10^{19}	1.80×10^{19}	1.0×10^{19}	5.0×10^{20}
Electron's thermal velocity (cm/s)	2.0×10^{7}	1.0×10^{7}	1.0×10^{7}	1.0×10^{7}
Hole's thermal velocity (cm/s)	1.0×10^{7}	1.0×10^{7}	1.0×10^{7}	1.0×10^{7}
Mobility of electrons (cm^2/Vs)	100	50	49	150
Mobility of hole (cm^2/Vs)	20	50	49	100
N_D for uniformly shallow donor concentration (cm^{-3})	1×10^{18}	1×10^{17}	0	0
N_A for uniformly shallow acceptor concentration (cm^{-3})	0	0	1×10^{18}	1.0×10^{18}
Density of defects (cm^{-3})	1.0×10^{14}	1.0×10^{14}	1.0×10^{14}	1.0×10^{14}

Using the Eqs. (1) & (2), the CBO and VBO were estimated [50, 51]. For V_2O_5 the CBO and VBO is-

$$\begin{aligned}\mathrm{CBO} &= \chi_{\mathrm{Absorber}} - \chi_{\mathrm{HTL}}\\ &= 4.20 - 3.40\\ &= 0.80\,\mathrm{ev}\end{aligned}$$

$$\begin{aligned}\mathrm{VBO} &= \chi_{\mathrm{HTL}} - \chi_{\mathrm{Absorber}} + \mathrm{Eg}_{(\mathrm{HTL})} - \mathrm{Eg}_{(\mathrm{Absorber})}\\ &= 3.40 - 4.20 + 2.20 - 1.58\\ &= -0.18\,\mathrm{ev}\end{aligned}$$

2.2 The Settings Used for Simulation and Numerical Modeling

The device under consideration was simulated using the global AM 1.5 spectrum at one solar illumination from the FTO (Fluorine-doped Tin Oxide) side at 300 K. In order to calculate the photovoltaic response of $CuSbS_2$-based solar panels, the physical characteristics of various layers and baseline parameters, which are crucial and ultimately determine the corresponding precision of simulated results, are chosen from experimental data, a variety of plausible estimates, or literature, and are listed in Table 1. The optical absorption spectra of the device in question, for its several layers SnS_2, $CuSbS_2$, and V_2O_5, are derived from previously published experimental data. Each semiconductor layer's bulk area is exposed to a single acceptor/donor-like bulk defect with a Gaussian energy distribution to reduce bulk recombination loss. Reasonable neutral interfacial flaws are included to account for losses resulting from minority carrier recombination at each contact, as indicated in Table 2.

Table 2 Parameters of interface used in the Al/FTO/SnS_2/$CuSbS_2$/Ni hetero junction solar panels

Parameters	V_2O_5/$CuSbS_2$ interface	$CuSbS_2$/SnS_2 interface
Type of defect	N	N
Electrons in a cross-sectional image (cm^2)	10^{-19}	10^{-19}
Holes in a captured cross section (cm^2)	10^{-19}	10^{-19}
Distribution of energy	S	S
Defect energy level reference E_t	Greater than the highest E_v	Greater than the highest E_v
Energy in connection with the reference (eV)	6.0×10^{-02}	6.0×10^{-02}
Density total (cm^{-2})	10^{10}	10^{10}

N.B, *n* neutral, *s* single

3 Outcomes and Discussion

3.1 Absorber ($CuSbS_2$) Layer Thickness and Carrier Concentration Effects on Solar Panel Performance

This section assesses the device's photovoltaic response by adjusting the $CuSbS_2$ layer's thickness and carrier concentration from 150 nm to 1650 nm and 10^{15} to 10^{22} cm^{-3}, respectively, while preserving the baseline values for all other material parameters for the various layers in Tables 1 and 2. Figure 2 displays the computational findings, or how the device's photovoltaic characteristics vary in response to variations in the concentration and thickness of the absorber layer. Figure 2 shows that, except for J_{SC}, all photovoltaic parameter values rise sharply until 450 nm, stabilize between 450 and 750 nm, and gradually increase as the $CuSbS_2$ layer thickness increases. Specifically, a thickness of only 900 nm yielded the maximum values of J_{SC}, V_{OC}, and PCE, mostly because of the $CuSbS_2$ layer's significant light absorption within the visible wavelengths. However, beyond 600 nm of absorber layer thickness, V_{OC} gradually drops because of increased recombination of carriers in the larger absorber

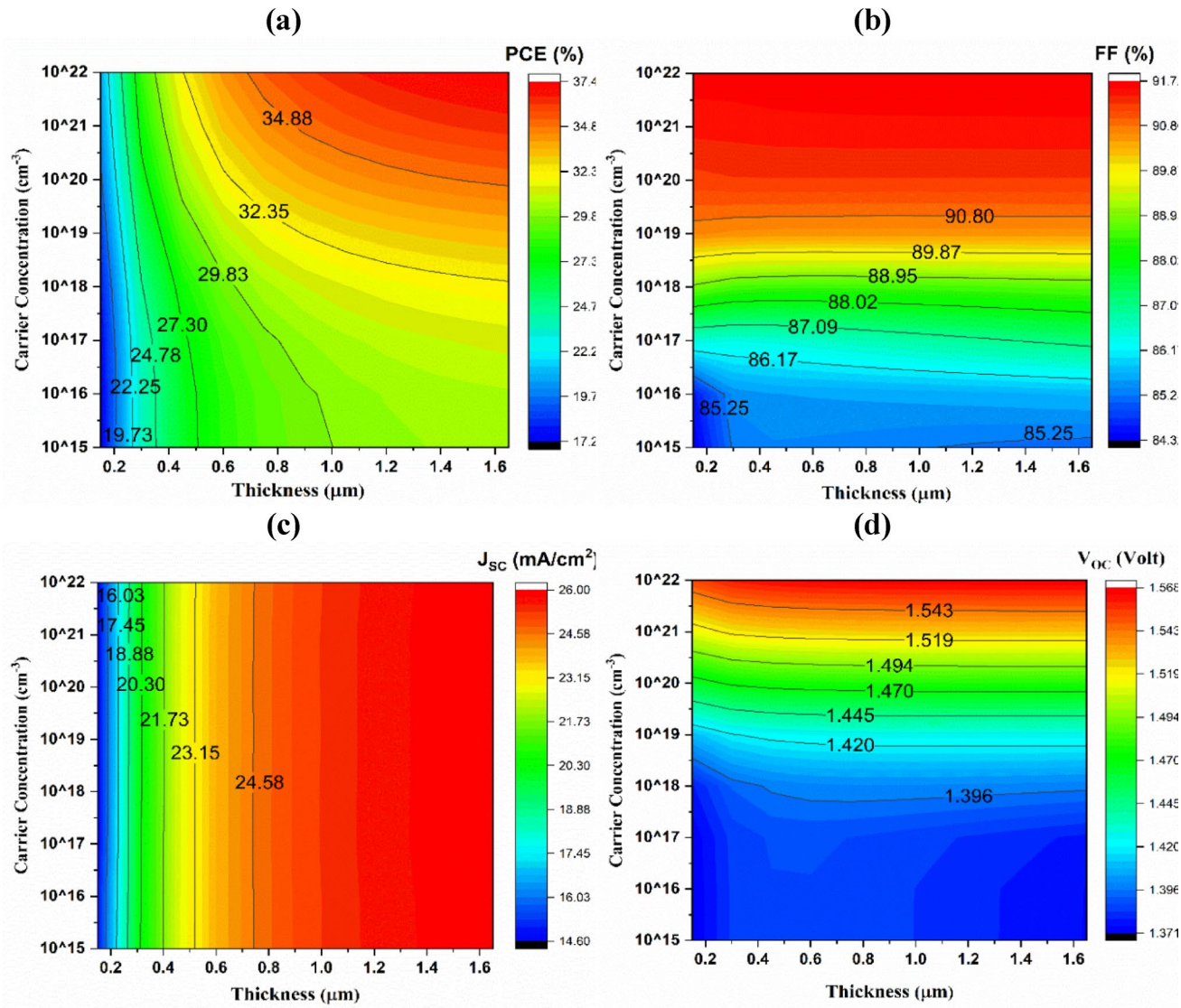

Fig. 2 The output characteristics of the photovoltaic panel **a** PCE, **b** FF, **c** J_{SC}, and **d** V_{OC} are affected by the thickness and carrier concentration of the active layer

layer. Beer-Lambert law states that more photons are absorbed within the device's absorber layer, which causes the first rise in J_{SC} with absorber thickness. Moreover, the initial rise in PCE results from the fact that most photogenerated carriers reach their electrodes before recombination occurs when the carriers' diffusion length is longer than the absorber layer thickness; as a result, PCE rises as the absorber layer thickness increases. PCE decreases as thickness increases, though, since bulk recombination takes place for the large absorber layer. The device's FF (Fill Factor) has a distinct pattern of decreasing value as absorber thickness grows, suggesting that series resistance rises as thickness increases. Future simulations based on first principles (ab initio) research can also be used to predict the ideal thickness of the absorber layer. The acceptor concentration (N_A) in the absorber layer has a major effect on the gadget's photovoltaic performance in addition to its thickness. The majority of the acceptor defects in the p-type $CuSbS_2$ combination originate during the synthesis of this substance and have a high density and low formation energy. Changing the amount of N_A in the $CuSbS_2$-absorber layer from 10^{15} to 10^{22} cm^{-3} allows one to comprehend how N_A affects the device's photovoltaic responses. The other material characteristics of the various layers remain constant. The variations in the devices' photovoltaic responses about the absorber layer's acceptor density fluctuation are shown in Fig. 2. Up to 1.0×10^{19} cm^{-3}, we see that V_{OC} grows linearly with N_A; after that, it dramatically declines as N_A increases.

The quasi-Fermi level of energy of holes decreases as N_A rises, increasing V_{OC} in the process. A further factor is

that when N_A rises, the device's built-in potential increases, improving the photogenerated separation of carriers in the SCR (Silicon Controlled Rectifier) and raising the Voc. Due to the increased recombination of carriers at the absorber, any additional rise in N_A caused a dramatic decrease in Voc. When N_A levels rose over a particular threshold, the device's J_{SC} also decreased. After a critical concentration, the improved carrier recombination reduces the minority carrier lifetime, which lowers the J_{SC}. This occurs because the photogenerated electrons' Coulomb interactions with the overcrowded acceptor doping may cause extra hole traps and interaction in the absorber layer [54]. The device's PCE rises as N_A increases due to the combined influence of V_{OC} and J_{SC}, reaching 1.0×10^{18} cm^{-3}. Controlling the absorber layer's acceptor concentration is crucial to run the device in the maximal PCE regime. $CuSbS_2$-based solar cells may attain a maximum PCE of around 31.09% with an absorber thickness of just 900 nm and an acceptor concentration of 1.0×10^{18} cm^{-3} (V_{OC} = 1.39 V, J_{SC} = 25.09 mA/cm^2, and FF = 88.54%). As a result, our study suggests that the $CuSbS_2$ absorber might be suitable for extremely thin solar photovoltaic systems.

3.2 The Impact of Active Layer Thickness and Density of Defects on the Functionality of the Single Absorber Device

The two primary photovoltaic processes that take place inside the absorber layer are generation and recombination. The kind and quantity of faults within the layer of absorption determine the measurement value of the absorption layer, which controls the device's efficiency. By altering the layer's density of defects from 10^{11} to 10^{17} cm^{-3}, while maintaining the other parameters listed in Table 1, it has been investigated how the density of flaws in the absorber layer impacts the photovoltaic cell. It is evident from Fig. 3's output plot that high output values are the consequence of low fault density. Each J-V parameter decreases as the density of the defect of the absorber layer increases. The values don't change until 10^{14} cm^{-3}, at which point they progressively decrease. Fault densities less than 10^{14} cm^{-3} are said to be irrelevant for lead-free electronics, and it would be extremely challenging to achieve them experimentally [55]. Therefore, as charge carrier recombination lowers, a lower defect density produces higher outputs. The ideal defect density for the simulation is 10^{14} cm^{-3}. An absorber device's efficiency is greatly influenced by the defect density in its active layers; higher defect densities result in noticeable decreases in J_{SC}, V_{OC}, FF, and eventually the PCE. The device's stability and performance can be improved by minimizing and resolving these problems. The active layer's thickness and defect density have a significant impact on how well $CuSbS_2$-based absorber devices work. The performance of solar cells may be greatly improved by adjusting these parameters, which makes $CuSbS_2$ a potential material for future photovoltaic applications. To reduce flaws and improve layer characteristics, future studies should concentrate on sophisticated manufacturing methods.

3.3 Effects of Concentration of Carrier and the Thickness of the V_2O_5 BSF Layer with SnS_2 ETL

This section aims to understand how the carrier densities of the ETL and BSF layers affect the device's photovoltaic response by varying them between 10^{14} and 10^{22} cm^{-3}, respectively. Other substance parameters are maintained at their baseline values while the simulation is run using the previously determined optimal absorber layer depth and carrier density. Figure 4 shows how the device's photovoltaic responses vary in response to variations in the ETL & BSF layer carrier densities. It is important to note that we also ran simulations to examine the effects of ETL & BSF layer thickness; the results are not displayed here. We discovered that the device's performance barely varies as the ETL and BSF thickness of layers increases.

Specifically, as the BSF layer thickness increases, all of the device's PV characteristics marginally rise as well. Conversely, as the degree of thickness of the ETL layer increases, the device's performance gradually declines. For the BSF and ETL layers, respectively, a thickness of 50 nm and 100 nm is selected to conduct more research. Figure 4a shows that as the ETL layer carrier concentration rises from 1.0×10^{14} to 1.0×10^{22} cm^{-3}, all of the device's photovoltaic parameters remain unchanged. The device is probably constrained by transport layers, recombination, or interface flaws if donor intensity is raised above an ideal threshold without improving photovoltaic characteristics. In these situations, passivation and interface engineering optimization are essential. But when the concentration of BSF layer carriers rises, the device's photovoltaic responses progressively improve until they reach saturation at concentrations higher than 1.0×10^{22} cm^{-3}. The proposed device's highest photovoltaic responses in this simulation are V_{OC}: 1.39 V, J_{SC}: 25.09 mA/cm^2, FF: 88.54%, and PCE: 31.09%, respectively, for the ETL and BSF layer carrier densities of 1.0×10^{17} cm^{-3} and 1.0×10^{18} cm^{-3}.

3.4 Defects at the $V_2O_5/CuSbS_2$ and $SnS_2/CuSbS_2$ Interfaces and their Impact on Device Performance

The characteristics that control how light and electricity interact can be changed by defects in a substance system. The effectiveness of the cell is also significantly impacted by the interface's quality. To look at how the number of

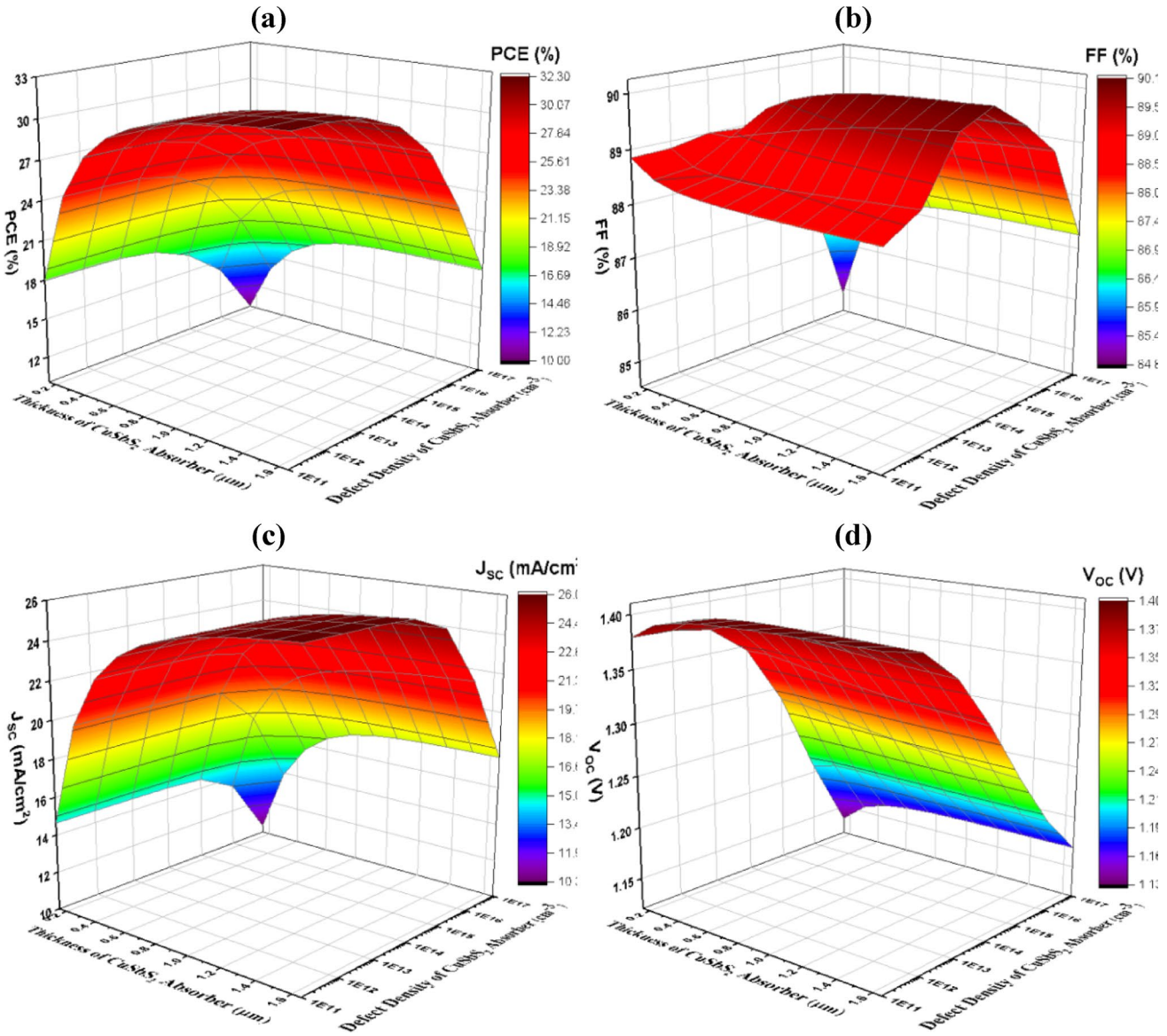

Fig. 3 The following PV performance characteristics are affected simultaneously by variations in absorber thickness and defect density of the FTO/SnS_2/$CuSbS_2$/V_2O_5 structure: **a** PCE, **b** FF, **c** J_{SC}, and **d** V_{OC}

interface defects affects the $CuSbS_2$-based photovoltaic cell's performance, Variations in the thicknesses of the CTSe absorbers from 150 to 1500 nm and the density of defects of the V_2O_5/$CuSbS_2$ and $CuSbS_2$/SnS_2 interfaces from 10^{10} to 10^{17} cm^{-2} are shown in Figs. 5 and 6, respectively. It is evident that when the concentration of defects at both interfaces increases, every performance feature of the gadget degrades. Specifically, the simulated findings show that all of the device's photovoltaic performance metrics are nearly steady until 10^{14} cm^{-2}, after which they steadily decline as the defect density rises. This decrease in performance results from an increase in the recombination of carriers at the contact point as the defect density rises [56, 57]. The device's series resistance dramatically rises in tandem with the growth of interfacial flaws [56].

As the density of defects at the SnS_2/$CuSbS_2$ interface increases from 10^{10} to 10^{17} cm^{-2}, the conversion efficiency decreases from 31.09 to 21.07%. At the V_2O_5/$CuSbS_2$ interface, however, the conversion efficiency decreases from 21.65 to 18.45% for the same increase in defect density. The output decline may be caused by the carriers' increased rate of recombination. Device performance will suffer when output values decrease due to increases in interface fault density levels [58]. The modeling findings demonstrate that faults at the buffer and absorber interface have a greater effect on the solar cell's performance than issues at the BSF and absorber interface [53]. Consequently, it is discovered

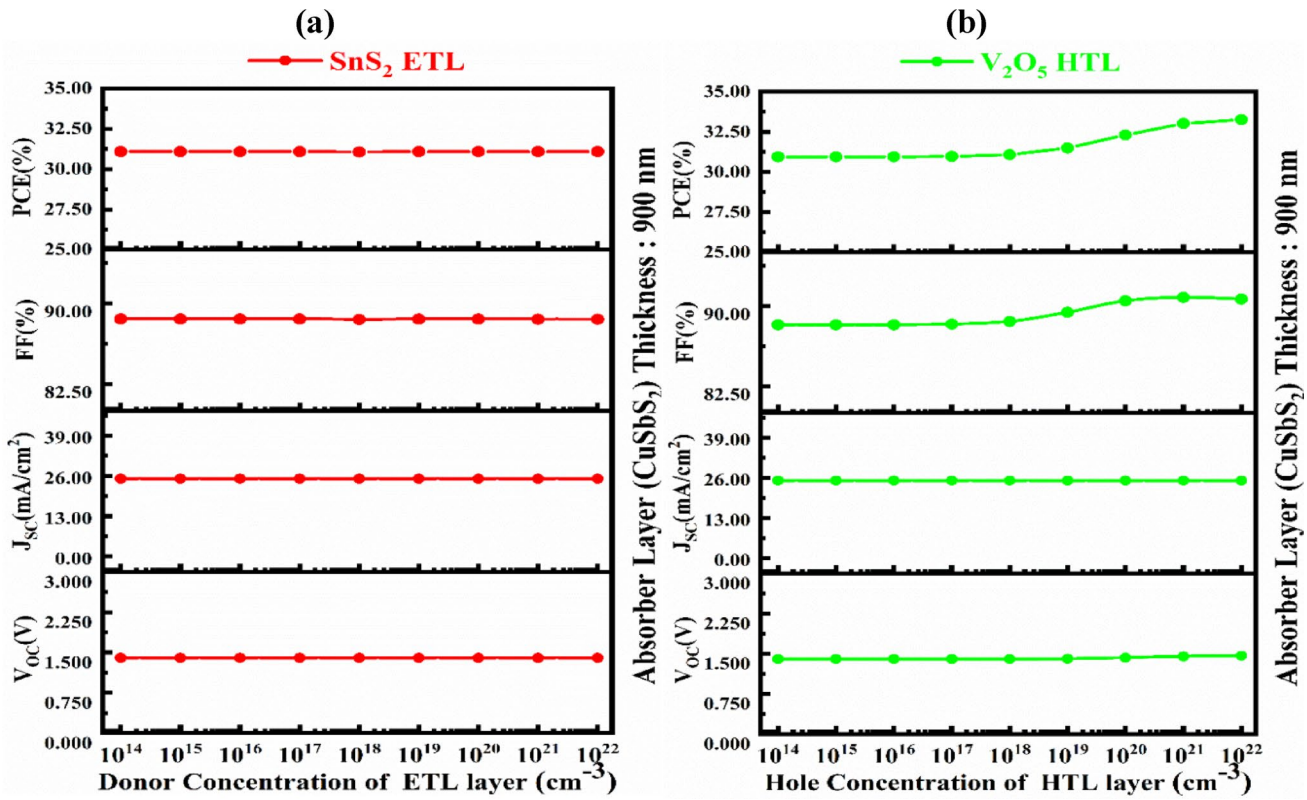

Fig. 4 $CuSbS_2$-based solar cells' PV responses in relation to **a** SnS_2 ETL and **b** the concentration of V_2O_5 BSF layer carriers

that the defect at the $SnS_2/CuSbS_2$ interface has a greater influence on the effectiveness of the suggested $CuSbS_2$ solar cell with heterojunction structure than does the defect at the $V_2O_5/CuSbS_2$ interface [59].

3.5 Impact of Thickness of Absorber Layer on the G-R Composition

The absorber layer's thickness can affect a $CuSbS_2$-based photovoltaic cell's recombination rate, total generation, hole density, and carrier electron density. Generally speaking, increasing the absorber layer thickness can enhance a solar cell's total generation. However, the effect on the recombination rate, the carrier density of electrons, and the concentration of holes may be more intricate and contingent upon several factors, such as the device design and material characteristics. As seen in Fig. 7a, the absorber layer thickness may have an impact on the recombination rate of a $CuSbS_2$-based solar cell. As thickness increases, so does the possibility of electron and hole pairs recombining, which might lower solar cell efficiency. The ideal absorber layer thickness must be selected to balance the generation and recombination rates to get the best performance. The total production of hole and electron pairs in a $CuSbS_2$-based photovoltaic cell may rise with the thickness of the absorber layer, as seen in Fig. 7b. This is done so that more photons may be absorbed by a larger absorber layer, enabling the creation of more hole-electron pairs. As mentioned before, the absorbers' thickness has a limit beyond which the pace of combination cannot increase without reducing the overall production. Figure 7c illustrates how the thickness of the absorber in a $CuSbS_2$-based photovoltaic cell may influence the hole concentration similarly to how it influences the carrier density of electrons. Because of the increased creation of electron-hole pairs, A larger hole density might be the result of a thicker absorber layer. However, recombination rates, which may differ based on the properties of the material and the design of the device, can also affect the hole density. In a $CuSbS_2$-based solar cell, the absorber layer thickness can affect the electron carrier density, as seen in Fig. 7d. Generally speaking, more photon absorption from a thicker layer of absorber can result in more pairs of electrons and holes and a higher electron carrier density. However, the possibility of hole-electron pairs recombining might also rise if the thickness exceeds a particular threshold. It can cause the electron carrier density to decrease. In conclusion, the overall thickness of the absorber can have a big influence on the efficiency of solar cells based on $CuSbS_2$. The absorber layer's thickness has a limit beyond which the rate of recombination might increase, reducing efficiency. This may lead to a rise in overall generation. Other elements of the device design, including the recombination rate, density

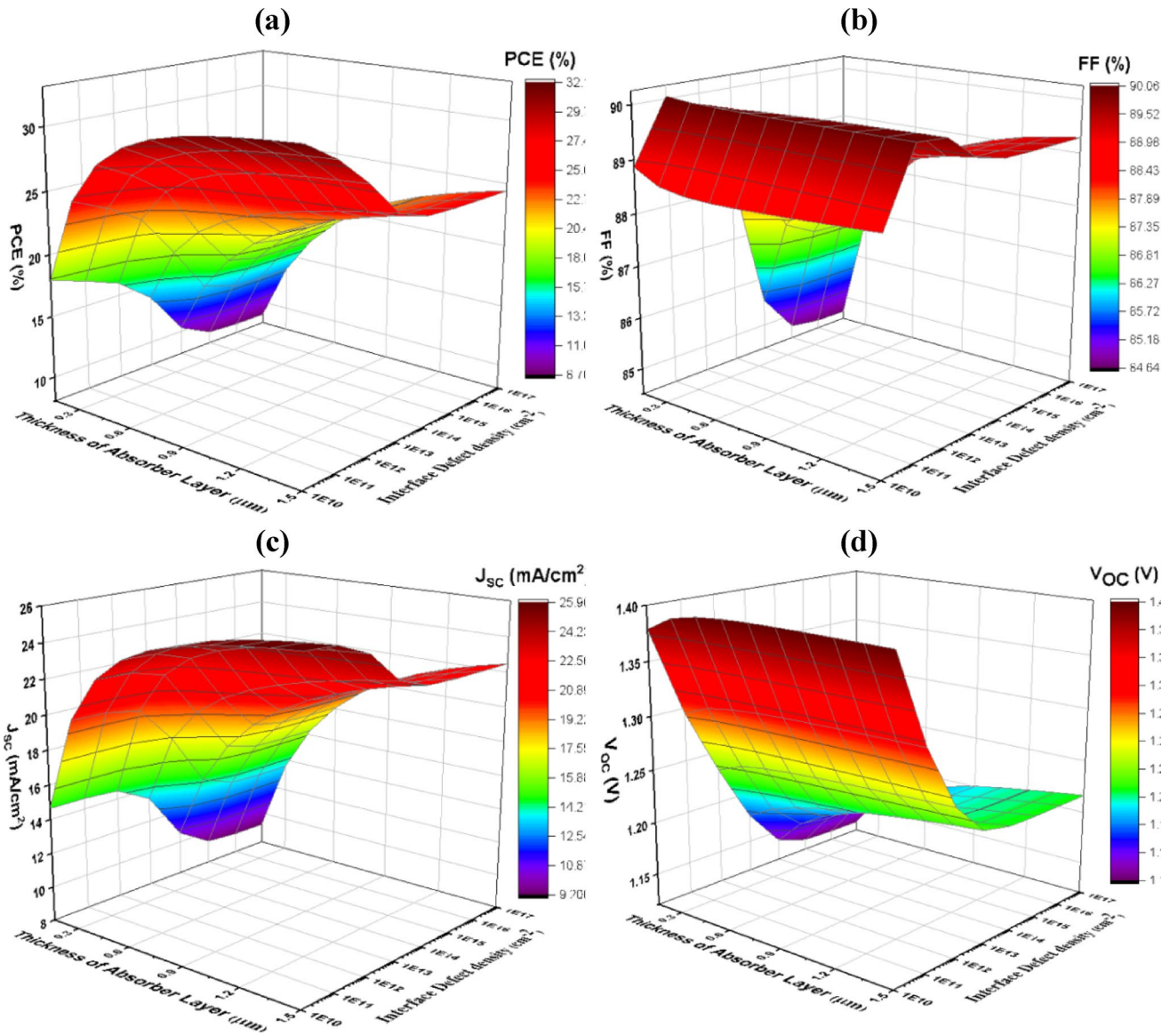

Fig. 5 Variations in solar efficiency characteristics according to absorber thickness and interface defect density at $V_2O_5/CuSbS_2$ interface **a** PCE, **b** FF, **c** J_{SC}, and **d** Voc

of electron carrier, and hole density, can also be affected by the absorber layer thickness.

3.6 Shunt and Series Resistance's Impact on the Optimized Device's Photovoltaic Parameters Response

Both shunt (R_{sh}) and series (R_s) resistance significantly affect the photovoltaic performance of heterojunction solar cells, because they jointly determine the J-V characteristics curve's appearance and slope. R_s originates from the electrical resistance associated with the semiconductors' contact and bulk resistance (BSF, ETL, and absorber layer). Shunt resistance, on the other hand, is mostly caused by several different carrier recombination pathways, such as defects in bulk materials and interfaces, and is also influenced by the device's architecture (cell edges effect) [60].

Thus, a higher Rs value will result in a lower J_{SC}, and a lower R_{sh} value will result in a lower V_{OC}, and together, these two factors cause the fill factor to drop precipitously, which lowers the PCE. This section examines how the Rs and R_{sh} function on the optimized device. We adjusted the shunt resistance in this simulation from 10 to 10^7 Ω·cm^2, and we also varied the R_s from 0 to 6 Ω·cm^2. Figure 8 displays the equivalent changes in the photovoltaic parameters. Figure 8 demonstrates that whereas V_{OC} first rises a little and subsequently tends to saturate as R_s increases, it continues to decline as shown for other photovoltaic parameters.

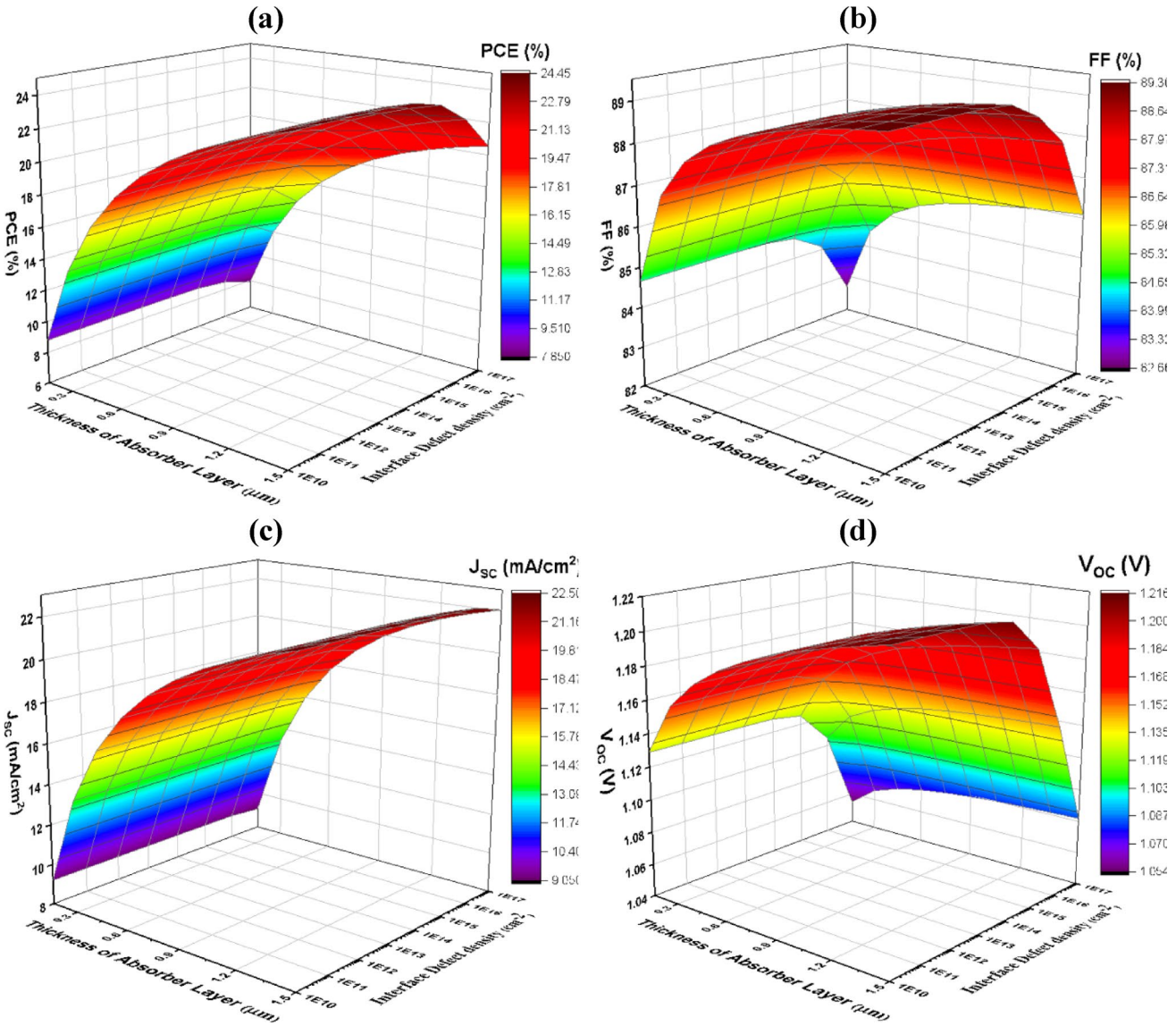

Fig. 6 Differences in photovoltaic efficiency properties as depending on the absorber's thickness and the interface defect density at $CuSbS_2/SnS_2$ interface **a** PCE, **b** FF, **c** J_{SC}, and **d** Voc

These results are entirely in line with the published literature [61]. It has been shown that FF degrades by over 2.6% for every 0.01 Ω rise in R_s, which is comparable to typical Si solar cells, which degrade by almost 2.5% for each 0.01 Ω rise in Rs. But it's important to see that even while the FF drops to 2.6%, the efficiency drops by a far smaller amount, just 0.92% while R_s rises by 0.01 Ω. Conversely, lowering R_{sh} below 1000 Ω·cm^2 will result in a sharp decline in all photovoltaic parameters Fig. 8. But when R_{sh} >1000 Ω·cm^2, PCE and additional photovoltaic metrics are less impacted.

3.7 The Absorber Layer Thickness of Affects the Q-E and J-V Solar Cells

One extremely promising substance for the absorber layer of solar cells is $CuSbS_2$. Quantum efficiency (Q-E) and density of current-voltage (J-V) and of the solar panel are strongly impacted by the thickness of the $CuSbS_2$ absorption layer. The J-V curve is produced by plotting the electrical density versus voltage over a $CuSbS_2$-based PV cell, as shown in Fig. 9a. More photons are absorbed when the $CuSbS_2$ absorption layer is thicker, which raises the photocurrent produced. Consequently, the J-V curve moved in the direction of larger current densities. However, some of the electron carriers generated may recombine before they reach the contacts if the absorber layer's surface is smooth,

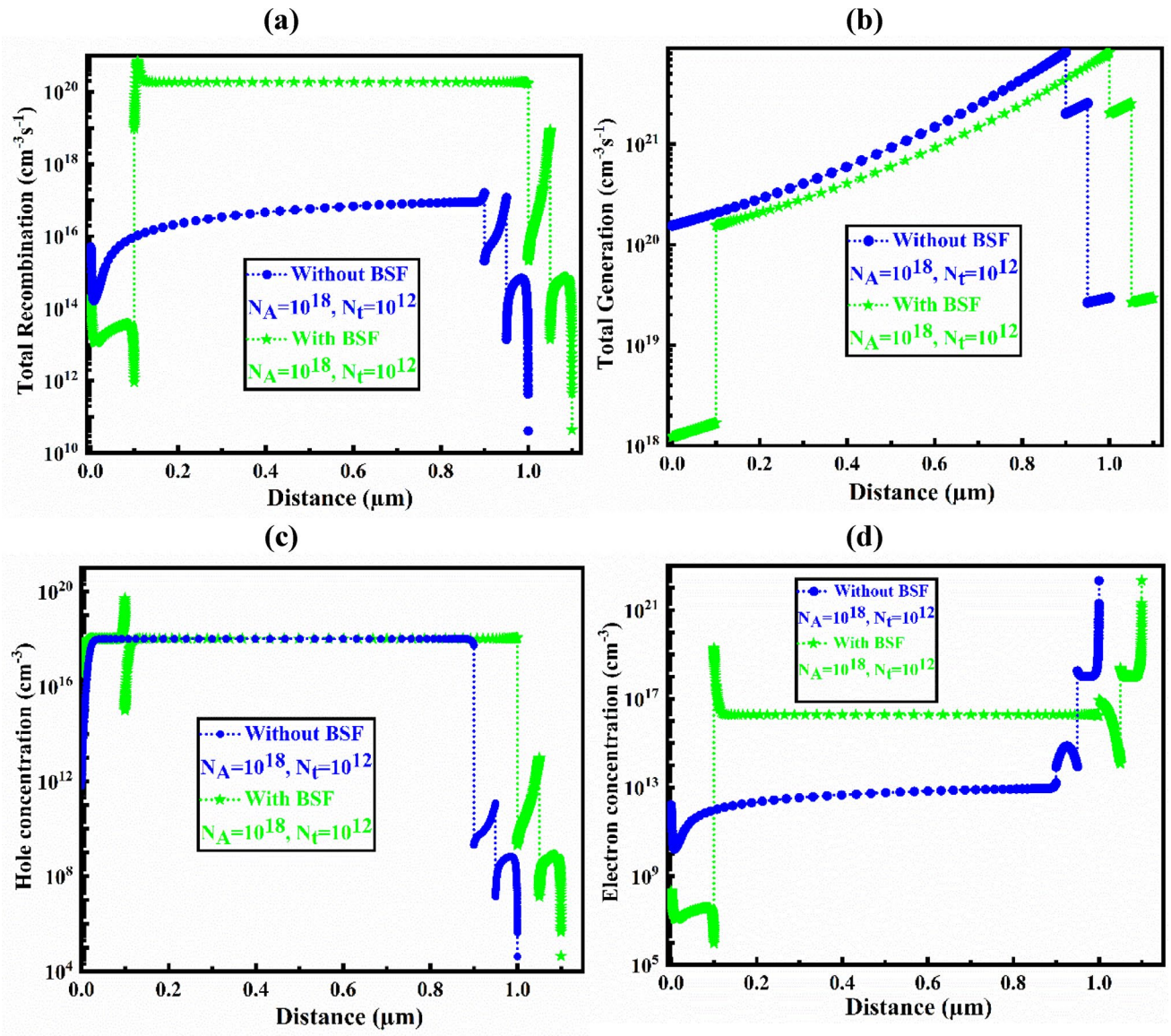

Fig. 7 Thickness of absorber layer effects on **a** recombination, **b** total generation, **c** hole density, and **d** electron carrier density

which would lower the solar cell's average PCE and Jsc [62]. Additionally, the $CuSbS_2$ absorber layer thickness affects a solar cell's Q-E. The quantity of captured particles in each incident quantum efficiency is a measure of the extent to which photons are converted into electrons. Photons with energy equal to or higher than the absorber layer's band gap have the greatest Q-E. Because of the increased absorption of photons, the Q-E initially increases as the $CuSbS_2$ absorption layer thickness grows. As the thickness grows, the Q-E finally reaches its maximum value, but as it does, it starts to decline due to carrier recombination in the bulk or at the highest point of the $CuSbS_2$ absorber layer. This optimization requires balancing the trade-off between increasing the J_{SC} and optimizing the Q-E. The optimal thickness may depend on the properties of the $CuSbS_2$ absorber layer's structure, the device's design, and the manufacturing procedure. Thus, the next study will concentrate on the absorber layer thickness of 900 nm with changed photovoltaic coefficients, where the maximum PCE of 31.09% was obtained.

3.8 The Effect of Temperature on a Cell's Functionality

The operating temperature of solar cells has a significant impact on their material characteristics and photovoltaic performance. Solar cells are frequently exposed to temperatures ranging from 288 to 323 K when they are placed outside [63] and in some other applications, even greater temperatures. To investigate the effects of temperature, the working temperature was raised from 275 to 475 K in this

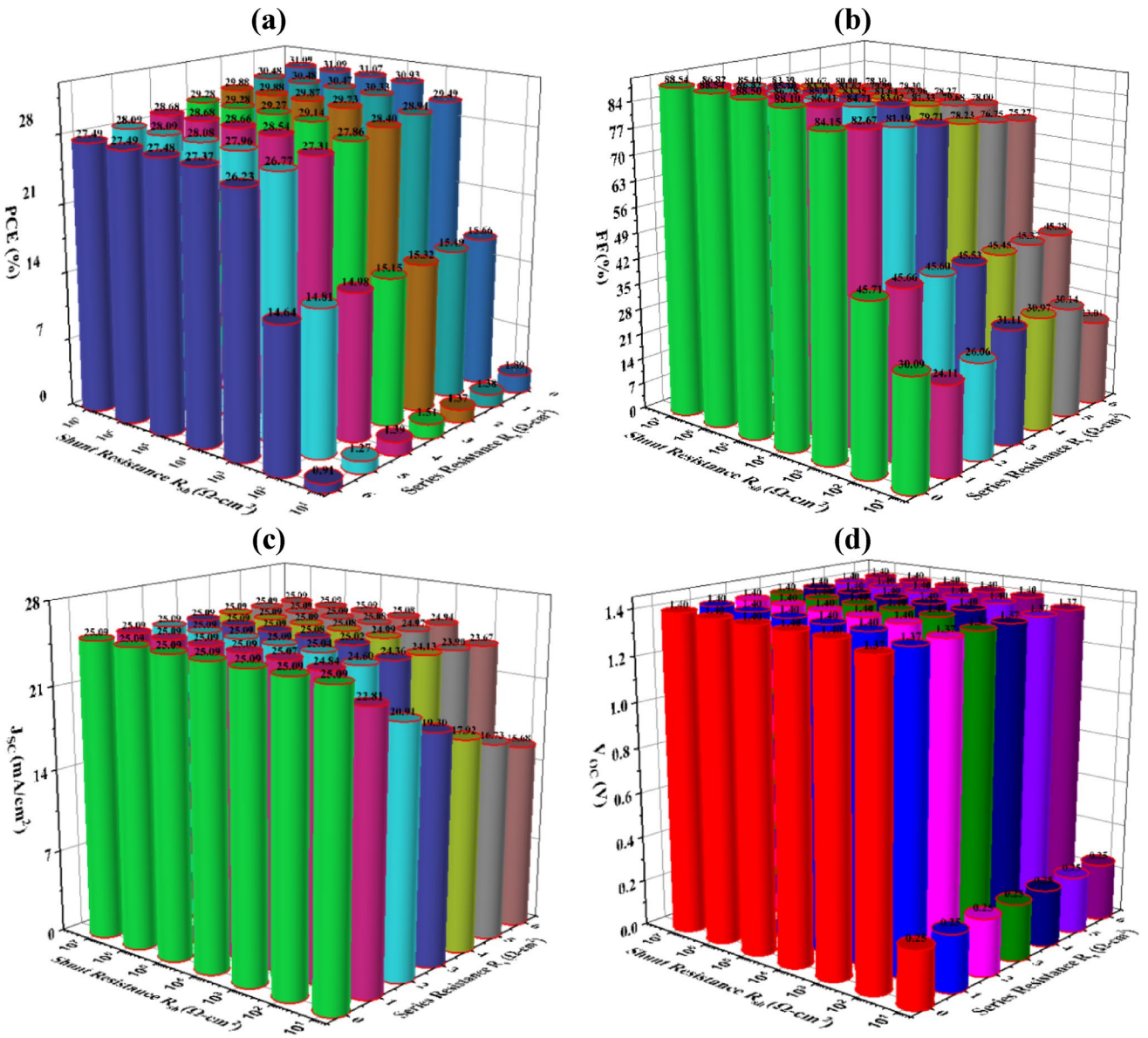

Fig. 8 $CuSbS_2$-based solar cells' photovoltaic parameters responses in relation to shunt resistance and series resistance

investigation. The main factor that largely affects the photovoltaic devices' PCE is their reverse saturation current density, which is influenced by the materials' temperature and band gap [64]. Figure 10 illustrates how $CuSbS_2$-based solar cells' performance is impacted by temperature. The device's normalized photovoltaic responses are displayed against the operational temperature variation in Fig. 10. As anticipated, a roughly linear decline in the FF and V_{OC} and a linear decline in the PCE are shown as the temperature rises. Before moving into the depletion area and gathering at the electrode, the drop in V_{OC} enables electrons to recombine with holes and acquire sufficient energy at higher temperatures [65]. There is a tiny increase in J_{SC}, which results from the semiconductor's band gap decreasing as temperature rises. However, the device's J_{SC} increased somewhat, which may have been brought on by heat generation [66]. Temperature changes result in changes in series resistance, which affect the material properties of the device, such as band gap, hole and electron concentration, and carrier mobility [67]. The ideal temperature for the device to get high cell efficiency is 300 K. Table 3 displays a comparison of the output metrics from this investigation with those from previous studies.

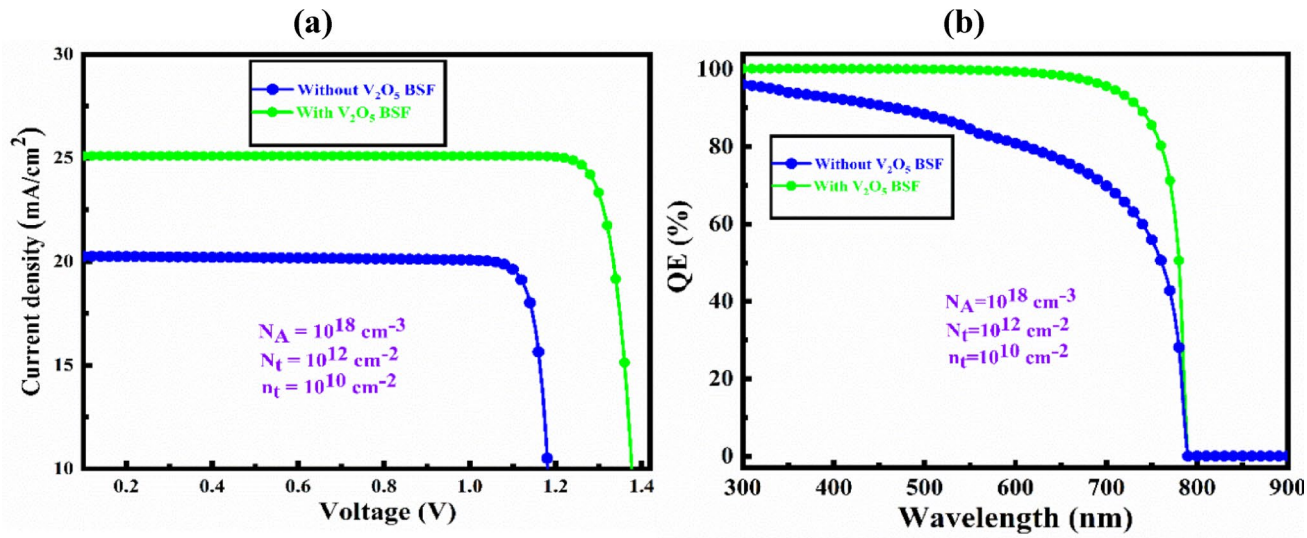

Fig. 9 **a** J-V & **b** Q-E characteristics of Al/FTO/SnS_2/$CuSbS_2$/V_2O_5/Ni heterojunction solar panel without and with BSF

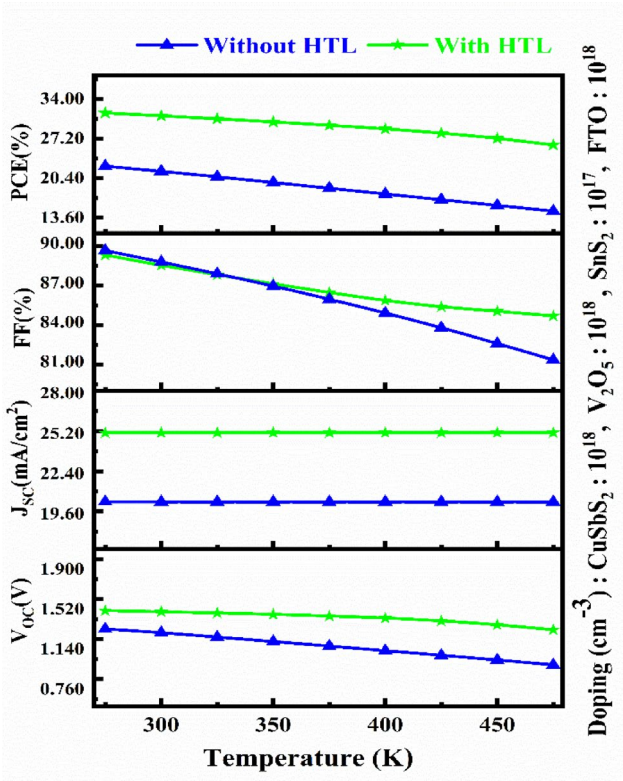

Fig. 10 The normalized operating temperature-dependent values of each photovoltaic performance indicator for CTSe-based solar cells with and without BSF

4 Enhancement of PSC Architecture Through Machine Learning

Recently, Machine Learning (ML) has become an essential instrument in photovoltaic research, providing sophisticated techniques for analyzing and enhancing solar cell performance. This work utilizes the Random Forest algorithm to forecast and evaluate the effects of diverse physical and material characteristics on photovoltaic performance, using its inherent feature significance method to identify the most significant qualities. This method assesses the importance of each parameter by measuring its impact on diminishing impurity at decision nodes, therefore identifying essential elements that influence device efficiency and stability. In some previous research investigates degradation mechanisms and design sensitivities in Copper Indium Gallium Selenide (CIGS) and lead-free perovskite ($FACsSnI_3$) thin-film solar cells by merging high-fidelity simulation data with hybrid machine learning models [69, 70]. Principal drivers of degradation, namely bulk and interfacial defects, TCO or AZO deterioration, and buffer-absorber discrepancies are methodically examined utilizing SCAPS-1D simulations and elucidated by various machine learning algorithms [71]. Those findings underscore the critical importance of buffer and absorber layer characteristics, along with carrier transport layers, in influencing overall efficiency.

In this study, the inherent feature is important in the strategy of the Random Forest method to identify the most significant characteristics affecting performance. This approach assesses the importance of each characteristic by quantifying its role in diminishing data impurity at each decision node in the tree. The decrease of impurities is measured by computing the MSE (Mean Squared Error) at each node, with these reductions then aggregated across all trees in the forest. The ultimate feature importance values are normalized to guarantee that their sum equals 100%, representing each feature's relative contribution to the model's predicted accuracy. The efficiency of photovoltaic devices is affected by a complex interaction of material and structural

Table 3 Comparison with similar simulation studies available in recent literature

Work type	Structures	J_{SC} (mA/cm^{-2})	V_{OC} (V)	FF (%)	PCE (%)	Refs.
T	Mo/$CuSbS_2$/CdS/n-ZnO/ITO/Al	30.61	701	57.61	12.37	[2]
T	Mo/$CuSbS_2$/TiO_2/ITO/Al	31.59	707	57.88	12.93	[2]
T	Ni(111)/$CuSbS_2$/TiO_2/ITO/Al	31.68	886	67.29	18.89	[2]
T	Au/$CuAlO_2$:Mg/$CuSbS_2$/TiO_2/ITO/Al	32.51	995	68.75	22.23	[2]
T	Au/$CuAlO_2$:Mg/$CuSbS_2$/TiO_2/ITO/Al	34.62	969	68.71	23.05	[2]
T	$CuSbS_2$/ZnS/ITO	24.11	1063	67.46	17.3	[35]
T	$CuSbS_2$/CdS/ZnO	28.25	919	81.01	21.09	[68]
T	Al/FTO/SnS_2/$CuSbS_2$/V_2O_5/Ni	25.09	1390	88.54	31.09	This work

T theoretical work

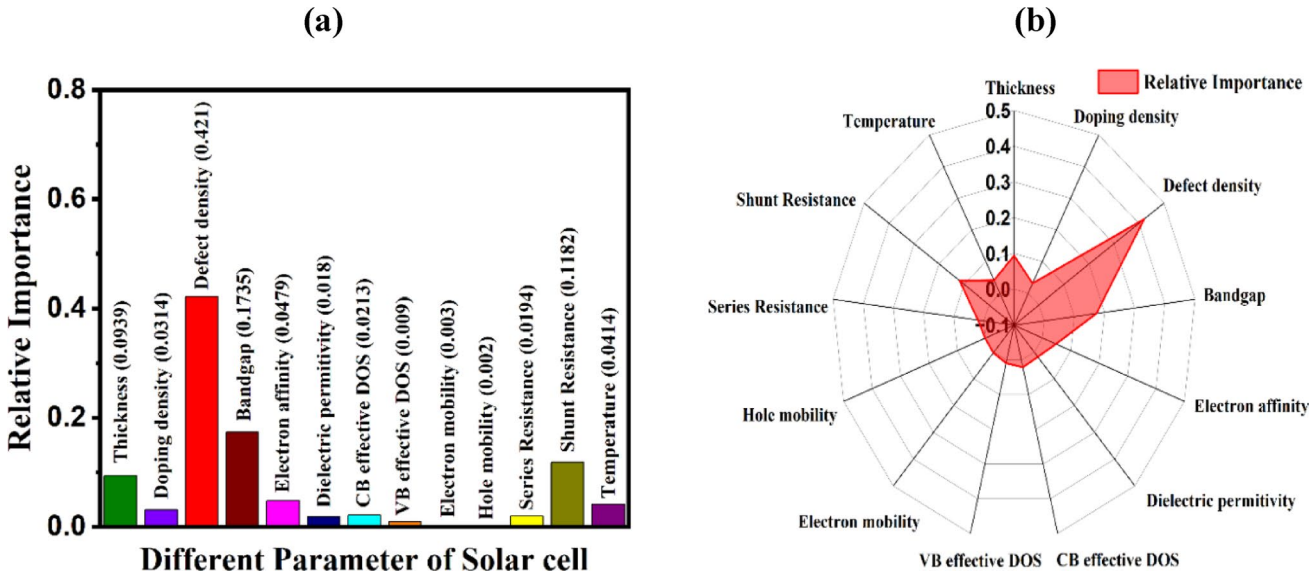

Fig. 11 **a** Bar and **b** radar charts illustrate key factors affecting the Al/FTO/SnS_2/$CuSbS_2$/V_2O_5/Ni solar cell's performance in the ML model

characteristics that frequently engage in non-linear relationships. Conventional models sometimes fail to accurately represent these complicated interactions, whereas machine learning algorithms are particularly adept at managing such intricacies. This study utilizes the Random Forest model to forecast PCE and assess the impact of each parameter on the device's performance. To build and verify the machine learning model for PV performance prediction, a comprehensive dataset of samples was created, each representing a unique combination of material and structural factors. Critical input factors that varied within the dataset encompassed optical and electrical parameters, including layer thickness, bandgap, charge carrier mobility, and material composition attributes recognized for their impact on photovoltaic performance. The dataset was methodically divided into 80% for training and 20% for testing, facilitating an initial assessment of the model's capacity to generalize to novel data. A Random Forest regression approach, chosen for its resilience in modelling intricate, nonlinear relationships, was trained with 230 estimators. The model did not explicitly utilize k-fold cross-validation; rather, the 80/20 split offered a statistically representative division adequate for first validation. Hyperparameter tuning was not performed using formal methods like grid search or random search; rather, standard parameters were utilized based on previous benchmarks [72], with the number of decision trees ($n = 100$) established to balance predictive stability and model complexity. Figure 11a, b illustrates the significance of each feature through bar and radar charts, offering a clear visual picture of the parameters' contributions to the model's overall predictive efficacy. Each axis in the radar map represents a distinct feature, and the displayed area indicates the degree to which each feature enhances the model's capacity to predict photovoltaic performance.

The comprehensive examination of the impact of diverse material and device characteristics on photovoltaic performance, indicating that Defect Density (42.1%), Bandgap (17.35%), and Shunt Resistance (11.82%) are the most significant factors. The essential parameters significantly influence the fundamental processes governing photovoltaic efficiency, with defect density being particularly critical, as elevated defect densities result in heightened recombination

losses, so directly diminishing the device's overall efficiency. The bandgap is a critical component that influences a material's capacity to absorb light and promote electrons to the conduction band, hence regulating its energy conversion potential. Conversely, shunt resistance is crucial in mitigating current leakage, so ensuring that a greater portion of the generated current traverses the external circuit, thereby augmenting the efficiency of the photovoltaic device. Other parameters, including Doping (3.14%), Thickness (9.39%), and Temperature (4.14%), have a relatively negligible impact, as they predominantly effect material conductivity, device stability, and operational dependability, rather than directly enhancing performance. Electron and hole mobility (0.3% and 0.2%) exert negligible influence, as these parameters affect charge transport and recombination losses; however, their contribution to performance increase is less significant than that of defect density, bandgap, and shunt resistance. The efficacy of the Random Forest method resides in its capacity to model and encapsulate the nonlinear, intricate interactions among numerous variables and their aggregate impact on PV efficiency. The technique employs an ensemble method by constructing many decision trees from random data subsets and aggregating their predictions, thereby adeptly managing the complexity of the data. Feature relevance ratings, obtained from the decrease in prediction error at each tree split, provide a definitive ranking of features according to their impact on photovoltaic performance. This method enables the identification of the primary parameters influencing photovoltaic efficiency, providing essential insights for the optimization of material characteristics and device configurations. The RFA's predictive skills identify parameters with little effects on efficiency, allowing researchers to concentrate on optimizing the most significant factors. Although the Random Forest method incurs considerable computational costs, it serves as an effective instrument for elucidating the complex, nonlinear correlations between material characteristics and photovoltaic performance, thereby enabling data-driven, focused optimisation strategies that can markedly enhance the design and efficiency of solar energy devices.

4.1 Analysis of Feature Importance Utilizing SHAP Values

This study utilizes SHAP values to elucidate the decision-making process of the model, pinpointing the principal aspects that affect the performance of photovoltaic devices. SHAP values provide a reliable and comprehensible method to measure the impact of individual features on the model's predictions. This work presents a SHAP summary graphic in Fig. 12, which visually illustrates the relative significance of each variable in predicting PV performance. Every point in the SHAP plot denotes the SHAP value of a certain feature for an individual data point. The x-axis of the figure illustrates the size of each feature's impact on the anticipated outcome, while the distribution of points indicates the variability of the feature's influence across different data points. The SHAP summary plot provides a detailed and data-centric analysis of the impact of various physical and material characteristics on PV device performance. Defect density emerges as the primary predictor (~42.1%), characterized by a wide and asymmetric SHAP distribution, signifying that the reduction of defects such as vacancies, dislocations, or grain boundaries directly improves charge transport, diminishes non-radiative recombination, and exerts a substantial positive influence on model predictions.

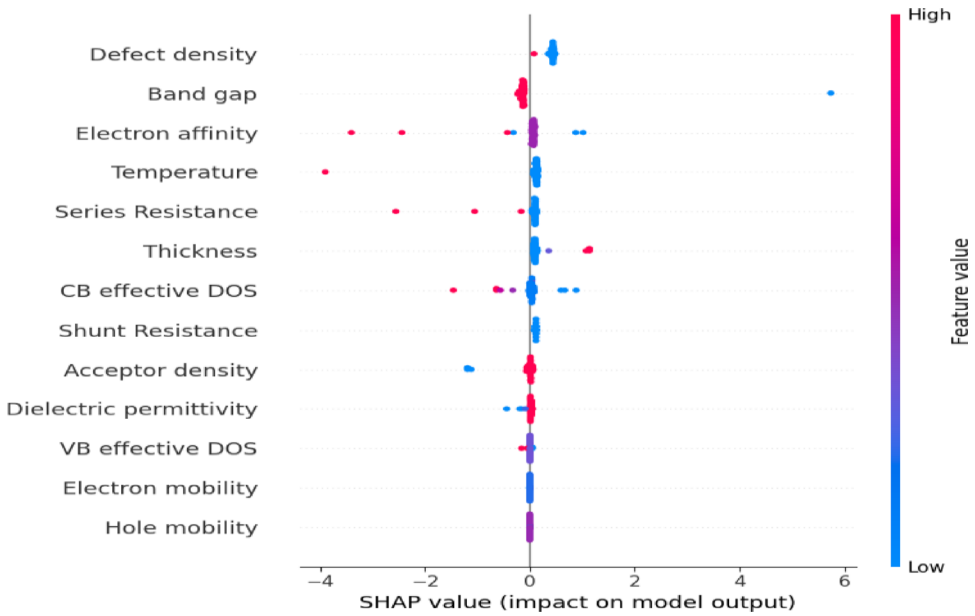

Fig. 12 The relative influence of non-correlated factors on device PCE is illustrated by SHAP values in a random forest regression model (organized by contribution)

Defect minimization is a paramount objective in materials engineering for high-efficiency solar cells. Bandgap energy (~17.35%) is a crucial characteristic, since ideal values enhance SHAP contributions by facilitating efficient solar spectrum absorption and reducing thermalization losses. The model indicates that both excessively tight and excessively wide bandgaps can adversely impact performance, underscoring the necessity of customizing material composition. Shunt resistance (~11.82%) is crucial; elevated resistance levels (shown by blue-to-purple dots with positive SHAP values) diminish leakage currents and enhance the FF and V_{OC}. The thickness (about 9.99%) exerts a moderate yet significant influence, as it impacts photon absorption depth and carrier collection excessively thin layers may diminish absorption, whereas overly thick layers may result in heightened recombination. Temperature (~4.14%) exerts a significant adverse impact, as elevated operating temperatures correlate with diminished SHAP values, illustrating the established decline in open-circuit voltage and overall efficiency resulting from thermally induced losses. Conversely, a set of characteristics comprising electron affinity, series resistance, acceptor density, dielectric constant, effective density of states in conduction and valence bands, and electron/hole mobilities exhibits very narrow SHAP value ranges concentrated around zero, indicating minimal independent predictive significance or overlapping influences with more prominent features. The color gradients and value distribution in the SHAP plot elucidate the correlation between feature magnitudes and their positive or negative effects, providing significant insights into parameter behavior throughout the dataset. The SHAP analysis clarifies the influence of each feature on solar cell performance and provides essential information for improving future photovoltaic device designs. It underscores that minimizing defect density, optimizing the bandgap, and controlling shunt resistance are essential for improving solar cell efficiency. Employing a data-driven approach like SHAP significantly enhances the transparency of machine learning models, aiding in the identification of critical parameters for device enhancement. This methodology establishes a clear foundation for future experimental initiatives, guiding the development of more efficient and reliable solar systems.

4.2 Assessment of Model Efficiency

The Random Forest method was utilized to forecast essential performance metrics of photovoltaic systems. To guarantee a comprehensive assessment of the model's predictive capability, the dataset was partitioned into two subsets: 80% for training and 20% for testing. This data partition is essential for evaluating the model's capacity to generalize to novel, unobserved data. Random Forest, an ensemble learning method, was chosen for its efficacy in simulating intricate, non-linear interactions commonly found in photovoltaic performance data. The model was trained with 100 decision trees, a configuration that mitigates the danger of overfitting while ensuring consistent and reliable predictions.

After training, the model's predictions for diverse solar cell parameters were juxtaposed with real simulation results. Scatter plots were created to evaluate the model's accuracy by comparing predicted and actual values for each parameter. Figure 13a–d exhibit robust linear correlations indicating that the model proficiently encapsulates the relationship between the predicted data and actual outputs. The aggregation of data points along the line of equality ($y=x$) further validates the model's predictive accuracy. The model's predictive efficacy was assessed using the coefficient of determination (R^2), which evaluates the extent to which the model accounts for the variance in the target variables. The R^2 values corresponding to each parameter are as follows:

R^2 values are 0.78 for PCE, 0.87 for V_{OC}, 0.89 for J_{SC}, and 0.82 for FF.

The R^2 value of 0.78 for PCE signifies that the model is moderately effective in accounting for the variance of this essential indicator of solar cell efficiency. The model exhibits good accuracy in predicting V_{OC}, evidenced by a R^2 value of 0.87, which significantly impacts the stability of V_{OC}. The R^2 value of 0.89 for J_{SC} indicates a strong match, albeit with minor imprecision, implying that the model captures primary trends while some variability may persist. The R^2 score of 0.82 for FF indicates the model's strong ability to predict this parameter, which is essential for assessing charge collection efficiency and overall device stability.

The machine learning model attains a notable mean accuracy of 84%, accompanied by a R^2 value of 0.84. The results underscore the Random Forest model's remarkable capacity to accurately predict photovoltaic performance, illustrating its efficacy in predicting the intricate and non-linear correlations inherent in photovoltaic device features. The low error rates and elevated R^2 values affirm the model's durability, establishing its dependability as an effective instrument for solar cell performance prediction and optimization.

5 Arrange for the Validation of Experiments

The experimental validation of the heterostructure Al/FTO/SnS_2/$CuSbS_2$/V_2O_5/Ni is planned in the following steps:

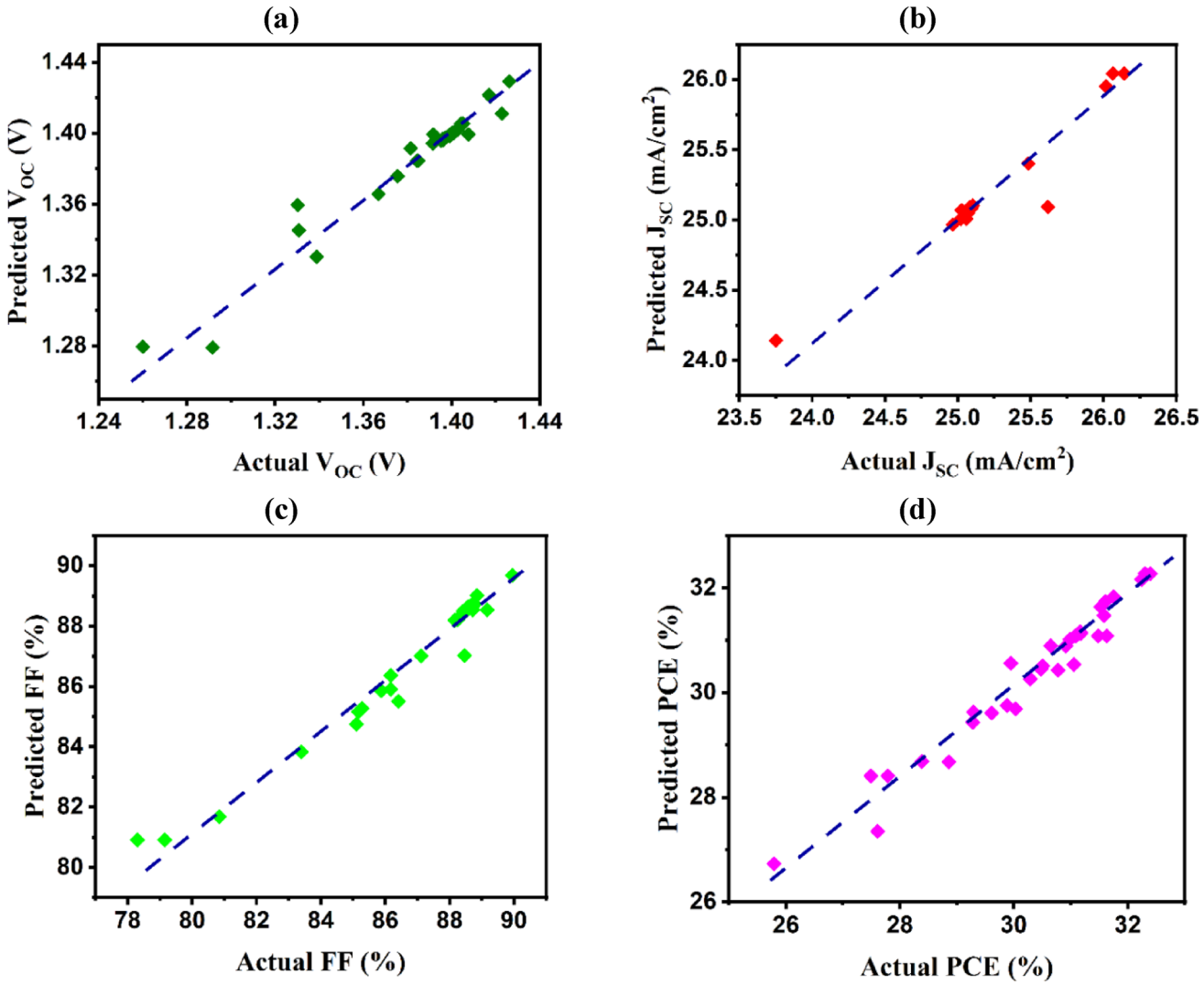

Fig. 13 Comparison of predicted and actual values for the Al/FTO/SnS_2/$CuSbS_2$/V_2O_5/Ni solar cell utilizing the machine learning model

5.1 Substrate Preparation (Al/FTO)

- Start with a glass that has been cleaned and coated with FTO (commercial or sputtered over Al if Al back contact is needed for).
- For around ten minutes each, ultrasonically agitate in detergent, DI water, acetone, and isopropanol.
- In order to improve surface wettability, dry under nitrogen and clean with UV-Ozone or plasma.

5.2 Deposition of SnS_2 Layer (ETL)

- Method: RF sputtering, spin-coating of the precursor solution, or chemical bath deposition (CBD).
- Conditions: Use precursors such as thioacetamide and $SnCl_4$.
- To enhance crystallinity, anneal at 300–350 °C in an environment rich in S or N.
- Characterization includes AFM (roughness), UV-Vis (bandgap), SEM (morphology), and XRD (phase).

5.3 Deposition of $CuSbS_2$ Absorber Layer

- Methods include sulfurization of the precursor, solution-based spin-coating (such as thiourea + metal salts), or co-evaporation.
- Annealing temperature: 350–400 °C in H_2S or sulfur vapor.
- Characterization includes Raman (phase purity), SEM/EDS (composition), XRD (crystallinity), and PL (defects).

5.4 Deposition of V_2O_5 Layer (BSF)

- Technique: RF sputtering, spin-coating of the V precursor, or thermal evaporation.
- Control Thickness: ~10–30 nm.
- Following a deposition Annealing: for stoichiometric V_2O_5, 200–300 °C in air.
- Characterization: AFM (interface quality), UPS (work function), and XPS (stoichiometry).

5.5 Top Electrode Deposition (Ni)

- Method: Sputtering, e-beam evaporation, or thermal evaporation.
- Masking: To specify the top contact shape, use a shadow mask.
- Thickness for ohmic contact: around 100 nm.
- Verify the contact quality and adhesion.

5.6 Structural and Morphological Characterization

- XRD: Every stage involves a phase analysis.
- Using top-view and cross-sectional imaging, SEM/EDS verifies the homogeneity and thickness of layers.
- AFM: Uniformity and roughness of the interface.
- TEM: Analysis of interfaces and grain boundaries (optional).

5.7 Optical and Electronic Characterization

- UV-Vis-NIR: Estimating absorption and bandgap.
- Photoluminescence (PL): The behavior of carrier recombination.
- UPS/XPS: Fermi level changes, work function, and band alignment.

5.8 Device Fabrication and I-V Testing

- Device Structure: Use a mask to define the active region, such as 0.1–1 cm².
- J–V Measurements: To calculate Voc, Jsc, FF, and efficiency, under AM1.5 light.
- Dark J–V: To examine shunt/leakage routes and diode quality.

5.9 External Quantum Efficiency (EQE)

- To validate wavelength-dependent photoresponse and each layer's contribution, measure EQE.

5.10 Stability Testing

- Humidity exposure, thermal cycling, and illumination soaking are used to assess long-term performance.
- Use EQE and periodic J-V measurements to monitor degeneration.

This process guarantees a comprehensive experimental validation of the structural and electrical properties of the Al/FTO/SnS_2/$CuSbS_2$/V_2O_5/Ni heterostructure.

6 Conclusions

This paper used SCAPS 1D software for simulation to investigate $CuSbS_2$-based heterojunction solar panels with environmentally friendly buffers and BSF layers. Al/FTO/n-SnS_2/p-$CuSbS_2$/p+-V_2O_5/Ni is a (n-p-p+) heterojunction solar cell structure that has been constructed and quantitatively examined. $CuSbS_2$/CdS heterojunction solar cells' weak PV performance has been considerably improved in this work by the addition of a V_2O_5 BSF layer and changing front and back contacts. The augmentation of built-in potential and decrease in back-contact recombination are responsible for this improvement in the device's performance. The $CuSbS_2$-based device structure has been modified by varying the density of carriers and layer thickness to optimize the PCE of the photovoltaic cell. The improved device is appropriate for ultra-thin solar photovoltaic devices as it exhibits a maximum PCE of 31.09% when the $CuSbS_2$ absorber layer's thickness is just 900 nm. Additionally, the study indicates that substituting Mo for Au as the back-contact material can boost the efficiency of innovative $CuSbS_2$ solar panels. In comparison to conventional $CuSbS_2$/CdS heterojunction solar cells, the solar cell's maximum efficiency, as determined by optimization, was 31.09% (V_{OC} = 1.39 V, J_{SC} = 25.09 mA/cm^2, FF = 88.54%), which is extremely encouraging. Additionally, a Random Forest Machine Learning algorithm predicts the optimum semiconductor parameters. The model quantifies each parameter's importance using SHAP values, revealing their contributions. The model predicts accurate performance and provides precise results with a mean correlation coefficient (R^2) of 84%. However, our study effectively illustrates the non-toxic, low-cost, and

plentiful $CuSbS_2$-based extremely thin solar panels as a viable option for the photovoltaic industry of the future.

Acknowledgements The authors are thankful to the Deanship of Graduate Studies and Scientific Research at University of Bisha for supporting this work through the Fast-Track Research Support Program.

Author Contributions Md. Abdul Monnaf, and Avijit Ghosh: Conceptualization, methodology, software, validation, formal analysis, visualization, investigation, data curation, supervision, writing—original draft, and review and editing.Asadul Islam Shimul, Mohammad Fokhrul Islam Buian, and Md Al Imran: Software, validation, formal analysis, investigation, data curation, writing—original draft, and review and editing.Qaium Hossain, Laboni Ferdoush, Anup Kumar Roy, Shahan Ahmed, Md Mahfuzur Rahman, Nondon Lal Dey, Aijaz Rasool Chaudhry: Software, validation, formal analysis, writing—original draft, and review and editing.

Data Availability No datasets were generated or analysed during the current study.

Declarations

Conflict of Interest The authors declare no competing interests.

Ethical Approval All the authors declare that the manuscript does not have studies on human subjects, human data or tissue, or animals.

References

1. C.A. Wolden et al., Photovoltaic manufacturing: present status, future prospects, and research needs. J. Vac. Sci. Technol. A, Vac. Surf. Films (2011). https://doi.org/10.1116/1.3569757
2. M.A. Rahman, Numerical modeling of ultra-thin CuSbS 2 heterojunction solar cell with TiO 2 electron transport and CuAlO 2:Mg BSF layers. Opt. Mater. Express. **12**(8), 2954 (2022). https://doi.org/10.1364/OME.465498
3. V.C. Karade et al., Combating open circuit voltage loss in Sb2Se3 solar cell with an application of SnS as a back surface field layer. Solar Energy **233**, 435–445 (2022). https://doi.org/10.1016/j.solener.2022.01.010
4. C. Candelise, M. Winskel, R. Gross, Implications for CdTe and CIGS technologies production costs of indium and tellurium scarcity. Prog. Photovolt. Res. Appl. **20**(6), 816–831 (2012). https://doi.org/10.1002/pip.2216
5. C. Booten, M. Mann, A. Momen, O. Abdelaziz, Critical material supply chain analysis: magnetocalorics, Golden, CO (United States). (2020). https://doi.org/10.2172/1659867
6. M. Green, E. Dunlop, J. Hohl-Ebinger, M. Yoshita, N. Kopidakis, X. Hao, Solar cell efficiency tables (version 57). Prog. Photovolt. Res. Appl. **29**(1), 3–15 (2021). https://doi.org/10.1002/pip.3371
7. T.D. Raju, V. Murugadoss, K.A. Nirmal, T.D. Dongale, A.V. Kesavan, T.G. Kim, Advancements in perovskites for solar cell commercialization: a review. Adv. Powder Mater. **4**(2), 100275 (2025). https://doi.org/10.1016/j.apmate.2025.100275
8. J. Zhou, G.-Q. Bian, Q.-Y. Zhu, Y. Zhang, C.-Y. Li, J. Dai, Solvothermal crystal growth of CuSbQ2 (Q=S, Se) and the correlation between macroscopic morphology and microscopic structure. J. Solid State Chem. **182**(2), 259–264 (2009). https://doi.org/10.1016/j.jssc.2008.10.025
9. A. Rabhi, M. Kanzari, B. Rezig, Optical and structural properties of CuSbS2 thin films grown by thermal evaporation method. Thin Solid Films **517**(7), 2477–2480 (2009). https://doi.org/10.1016/j.tsf.2008.11.021
10. Y. Rodríguez-Lazcano, M.T.S. Nair, P.K. Nair, CuSbS2 thin film formed through annealing chemically deposited Sb2S3–CuS thin films. J. Cryst. Growth. **223**(3), 399–406 (2001). https://doi.org/10.1016/S0022-0248(01)00672-8
11. S.H. Pawar, A.J. Pawar, P.N. Bhosale, Spray pyrolytic deposition of CuBiS2 thin films. Bull. Mater. Sci. **8**(3), 423–426 (1986). https://doi.org/10.1007/BF02744156
12. P. Sonawane, P. Wani, L. Patil, T. Seth, Growth of CuBiS2 thin films by chemical bath deposition technique from an acidic bath. Mater. Chem. Phys. **84**, 2–3 (2004). https://doi.org/10.1016/S0254-0584(03)00221-9
13. L. Yu, A. Zunger, Identification of potential photovoltaic absorbers based on first-principles spectroscopic screening of materials. Phys. Rev. Lett. **108**(6), 068701 (2012). https://doi.org/10.1103/PhysRevLett.108.068701
14. J.T.R. Dufton, A. Walsh, P.M. Panchmatia, L.M. Peter, D. Colombara, M.S. Islam, Structural and electronic properties of CuSbS2 and CuBiS2: potential absorber materials for thin-film solar cells. Phys. Chem. Chem. Phys. **14**(20), 7229 (2012). https://doi.org/10.1039/c2cp40916j
15. M. Kumar, C. Persson, CuSbS2 and CuBiS2 as potential absorber materials for thin-film solar cells. J. Renew. Sustain. Energy (2013). https://doi.org/10.1063/1.4812448
16. J. Heo, G. Laurita, S. Muir, M.A. Subramanian, D.A. Keszler, Supporting Information for enhanced thermoelectric performance of synthetic tetrahedrites, p. 1–10
17. D. Chen et al., Thermoelectric enhancement of ternary copper chalcogenide nanocrystals by magnetic nickel doping. Adv. Electron. Mater. **2**, 2–6 (2016). https://doi.org/10.1002/aelm.201500473
18. S. Dekhil, H. Dahman, S. Rabaoui, N. Yaacoub, L.E. Mir, Investigation on microstructural and optical properties of CuSbS2 nanoparticles synthesized by hydrothermal technique. J. Mater. Sci. Mater. Electron. **28**(16), 11631–11635 (2017). https://doi.org/10.1007/s10854-017-6965-8
19. V. Vinayakumar et al., Cusbs2 thin films by rapid thermal processing of Sb2S3-Cu stack layers for photovoltaic application. Solar Energy Materials and Solar Cells **164**, 19–27 (2017). https://doi.org/10.1016/j.solmat.2017.02.005
20. L. Shi, C. Wu, J. Li, J. Ding, Selective synthesis and photoelectric properties of Cu3SbS4 and CuSbS2 nanocrystals. J. Alloys Compd. **694**, 132–135 (2017). https://doi.org/10.1016/j.jallcom.2016.09.307
21. L. Wan et al., Two-stage co-evaporated CuSbS2 thin films for solar cells. J. Alloys Compd. **680**, 182–190 (2016). https://doi.org/10.1016/j.jallcom.2016.04.193
22. J.A. Ramos Aquino, D.L. Rodriguez Vela, S. Shaji, D.A. Avellaneda, B. Krishnan, Spray pyrolysed thin films of copper antimony sulfide as photovoltaic absorber. Phys. Status Solidi C. **13**(1), 24–29 (2016). https://doi.org/10.1002/pssc.201510102
23. R.E. Ornelas-Acosta, D. Avellaneda, S. Shaji, G.A. Castillo, T.K. Das Roy, B. Krishnan, CuSbS2 thin films by heating Sb2S3/Cu layers for PV applications. J. Mater. Sci. Mater. Electron. **25**(10), 4356–4362 (2014). https://doi.org/10.1007/s10854-014-2173-y
24. S. Banu, S.J. Ahn, S.K. Ahn, K. Yoon, A. Cho, Fabrication and characterization of cost-efficient CuSbS2 thin film solar cells using hybrid inks. Sol. Energy Mater. Sol. Cells. **151**, 14–23 (2016). https://doi.org/10.1016/j.solmat.2016.02.013
25. W. Septina, S. Ikeda, Y. Iga, T. Harada, M. Matsumura, Thin film solar cell based on CuSbS2 absorber fabricated from an electrochemically deposited metal stack. Thin Solid Films. **550**, 700–704 (2014). https://doi.org/10.1016/j.tsf.2013.11.046

26. S.C. Riha, A.A. Koegel, J.D. Emery, M.J. Pellin, A.B.F. Martinson, Low-temperature atomic layer deposition of CuSbS 2 for thin-film photovoltaics. ACS Appl. Mater. Interfaces **9**(5), 4667–4673 (2017). https://doi.org/10.1021/acsami.6b13033
27. S. Dekhil, H. Dahman, F. Ghribi, H. Mortada, N. Yaacoub, L.E. Mir, Study of CuSbS 2 thin films nanofibers prepared by spin coating technique using ultra pure water as a solvent. Mater. Res. Express **6**(8), 086450 (2019). https://doi.org/10.1088/2053-1591/ab24f6
28. O.Y. Ramírez-Esquivel, Z. Montiel-González, A.M. Garay-Tapia, M.C. Barrero-Moreno, F.S. Aguirre-Tostado, D.A. Mazón-Montijo, Mechanisms of phase evolution in the Cu–Sb–S system controlled by the incorporation of Cu in Sb 2 S 3 thin films. ACS Appl. Mater. Interfaces. **17**(1), 1615–1626 (2025). https://doi.org/10.1021/acsami.4c17960
29. J. van Embden, J.O. Mendes, J.J. Jasieniak, A.S.R. Chesman, E. Della Gaspera, Solution-processed CuSbS 2 thin films and superstrate solar cells with CdS/In 2 S 3 buffer layers. ACS Appl. Energy Mater. **3**(8), 7885–7895 (2020). https://doi.org/10.1021/acsaem.0c01296
30. Y. Rodríguez-Lazcano, M.T.S. Nair, P.K. Nair, Photovoltaic p-i-n structure of Sb[sub 2]S[sub 3] and CuSbS[sub 2] absorber films obtained via chemical bath deposition. J. Electrochem. Soc. (2005). https://doi.org/10.1149/1.1945387
31. F.W. de Souza, Effects of thermochemical treatment on CuSbS 2 photovoltaic absorber quality and solar cell reproducibility. J. Phys. Chem. C **120**, 18377–18385 (2016). https://doi.org/10.1021/acs.jpcc.6b04206
32. C. Macías et al., Thin film solar cell based on CuSbS 2 absorber prepared by chemical bath deposition (CBD). Mater. Res. Bull. **87**, 161–166 (2017). https://doi.org/10.1016/j.materresbull.2016.11.028
33. A.W. Welch et al., Accelerated development of CuSbS 2 thin film photovoltaic device prototypes. Prog. Photovoltaics Res. Appl. **24**(7), 929–939 (2016). https://doi.org/10.1002/pip.2735
34. Y. Zhang et al., High open-circuit voltage CuSbS 2 solar cells achieved through the formation of epitaxial growth of CdS/CuSbS 2 hetero-interface by post-annealing treatment. Prog. Photovoltaics Res. Appl. **27**(1), 37–43 (2019). https://doi.org/10.1002/pip.3061
35. Sadanand, D.K. Dwivedi, Modeling of photovoltaic solar cell based on $CuSbS_2$ absorber for the enhancement of performance. IEEE Trans. Electron. Devices. **68**(3), 1121–1128 (2021). https://doi.org/10.1109/TED.2020.3048326
36. T.J. Whittles et al., Core levels, band alignments, and valence-band states in $CuSbS_2$ for solar cell applications. ACS Appl. Mater. Interfaces **9**(48), 41916–41926 (2017). https://doi.org/10.1021/acsami.7b14208
37. T. Minemoto et al., Theoretical analysis of the effect of conduction band offset of window/CIS layers on performance of CIS solar cells using device simulation. Sol Energy Mater. Sol Cells. **67**, 1–4 (2001). https://doi.org/10.1016/S0927-0248(00)00266-X
38. H. Han, X. Zhao, J. Liu, Enhancement in photoelectric conversion properties of the dye-sensitized nanocrystalline solar cells based on the hybrid TiO[sub 2] electrode. J. Electrochem. Soc. **152**(1), A164 (2005). https://doi.org/10.1149/1.1828245
39. M. Ghaleb, A. Arrar, Z. Touaa, Optimization and performance analysis of a TiO_2/*i*-$CH_3NH_3SnBr_3$/$CsPbI_3$/Al(BSF) heterojunction perovskite solar cell for enhanced efficiency. ACS Omega **8**(40), 37011–37022 (2023). https://doi.org/10.1021/acsomega.3c03891
40. Y. Zhang, Z. Liu, D. Zang, L. Feng, Structural and opto-electrical properties of Cu–Al–O thin films prepared by magnetron sputtering method. Vacuum. **99**, 160–165 (2014). https://doi.org/10.1016/j.vacuum.2013.05.019
41. K.A. Nirmal, T.D. Dongale, S.S. Sutar, A.C. Khot, T.G. Kim, Machine learning empowers efficient design of ternary organic solar cells with PM6 donor. J. Energy Chem. **100**, 337–347 (2025). https://doi.org/10.1016/j.jechem.2024.08.052
42. V.C. Karade et al., Unraveling the effect of compositional ratios on the kesterite thin-film solar cells using machine learning techniques. Crystals. **13**(11), 1–10 (2023). https://doi.org/10.3390/cryst13111581
43. V.C. Karade et al., Machine learning assisted analysis, prediction, and fabrication of high-efficiency CZTSSe thin film solar cells. Adv. Funct. Mater. **33**, 1–11 (2023). https://doi.org/10.1002/adfm.202303459
44. D.A. Clugston, P.A. Basore, PC1D version 5: 32-bit solar cell modeling on personal computers, in *Conference Record of the Twenty Sixth IEEE Photovoltaic Specialists Conference*, (1997), p. 207–210. https://doi.org/10.1109/PVSC.1997.654065
45. M. Elbar, S. Tobbeche, Numerical simulation of CGS/CIGS single and tandem thin-film solar cells using the Silvaco-Atlas software. Energy Procedia. **74**, 1220–1227 (2015). https://doi.org/10.1016/j.egypro.2015.07.766
46. S. Geißendörfer, S. Geißendörfer, J. Lacombe, G. Letay, K. Von Maydell, C. Agert, Simulation of amorphous and microcrystalline thin film silicon solar cells with sentaurus TCAD simulation of amorphous and microcrystalline thin film silicon solar cells with Sentaurus TCAD modeling with TCAD single and Tandem solar cells (1-dim) The au, no. September, (2010), p. 14–15. https://doi.org/10.4229/25thEUPVSEC2010-3AV.1.86
47. Y. Liu, Y. Sun, A. Rockett, A new simulation software of solar cells—wxAMPS. Sol. Energy Mater. Sol. Cells **98**, 124–128 (2012). https://doi.org/10.1016/j.solmat.2011.10.010
48. M. Burgelman, J. Verschraegen, S. Degrave, P. Nollet, Modeling thin-film PV devices. Prog. Photovoltaics Res. Appl. (2004). https://doi.org/10.1002/pip.524
49. H. Zhu, A.K. Kalkan, J. Hou, S.J. Fonash, Applications of AMPS-1D for solar cell simulation, in *AIP Conference Proceedings*, (1999), p. 309–314. https://doi.org/10.1063/1.57978
50. A. Kuddus, S.K. Mostaque, J. Hossain, Simulating the performance of a high-efficiency SnS-based dual-heterojunction thin film solar cell. Opt. Mater. Express. **11**(11), 3812 (2021). https://doi.org/10.1364/OME.439629
51. M.A. Monnaf, A.K.M.M. Haque, M.H. Ali, S. Bhattarai, M.D. Haque, M.F. Rahman, Design and simulation of Cu 2 SnSe 3 -based solar cells using various hole transport layer (HTL) for performance efficiency above 32%. Phys. Scr. **98**(12), 125903 (2023). https://doi.org/10.1088/1402-4896/ad0529
52. M.F. Rahman, M.A. Monnaf, M. Amami, L. Ben Farhat, M.A. Rahman, Improving the efficiency above 35% of MoS2-based solar cells by through optimization of various wide-bandgap S-chalcogenides ETL. J. Phys. Chem. Solids **194**, 112216 (2024). https://doi.org/10.1016/j.jpcs.2024.112216
53. M.A. Monnaf, A.K.M.M. Haque, M.H. Ali, S. Bhattarai, M.D. Haque, M.F. Rahman, Design and simulation of Cu2SnSe3-based solar cells using various hole transport layer (HTL) for performance efficiency above 32%. Phys. Scr. (2023). https://doi.org/10.1088/1402-4896/ad0529
54. M. Djinkwi Wanda, S. Ouédraogo, F. Tchoffo, F. Zougmoré, J.M.B. Ndjaka, Numerical investigations and analysis of Cu 2 ZnSnS 4 based solar cells by SCAPS-1D. Int. J. Photoenergy **2016**, 1–9 (2016). https://doi.org/10.1155/2016/2152018
55. S. Taheri, A. Ahmadkhan kordbacheh, M. Minbashi, A. Hajjiah, Effect of defects on high efficient perovskite solar cells. Opt. Mater. (Amst) **111**, 110601 (2021). https://doi.org/10.1016/j.optmat.2020.110601
56. J. Tao et al., Investigation of electronic transport mechanisms in *Sb2Se3* thin-film solar cells. Sol. Energy Mater. Sol. Cells **197**, 1–6 (2019). https://doi.org/10.1016/j.solmat.2019.04.003

57. Y. Xiao, H. Wang, H. Kuang, Numerical simulation and performance optimization of Sb2S3 solar cell with a hole transport layer. Opt. Mater. (Amst) **108**, 110414 (2020). https://doi.org/10.1016/j.optmat.2020.110414
58. I. Mohanty, S. Mangal, U.P. Singh, Performance optimization of lead free-MASnI3/CIGS heterojunction solar cell with 28.7% efficiency: a numerical approach. Opt. Mater. (Amst). **122**(PB), 111812 (2021). https://doi.org/10.1016/j.optmat.2021.111812
59. Z. Gu et al., Novel planar heterostructure perovskite solar cells with CdS nanorods array as electron transport layer. Sol. Energy Mater. Sol. Cells **140**, 396–404 (2015). https://doi.org/10.1016/j.solmat.2015.04.015
60. S.R. Rummel, T.J. McMahon, Effect of cell shunt resistance on PV module performance at reduced light levels, in *AIP Conference Proceedings*, vol. 353 (1996), p. 581–586. https://doi.org/10.1063/1.49388
61. M.M. Khatun, A. Sunny, S.R. Al Ahmed, Numerical investigation on performance improvement of WS2 thin-film solar cell with copper iodide as hole transport layer. Sol. Energy **224**, 956–965 (2021). https://doi.org/10.1016/j.solener.2021.06.062
62. M.F. Rahman et al., Concurrent investigation of antimony chalcogenide (Sb2Se3 and Sb2S3)-based solar cells with a potential WS2 electron transport layer. Heliyon. **8**(12), e12034 (2022). https://doi.org/10.1016/j.heliyon.2022.e12034
63. D.C. Northrop, *Book review: Semiconductor devices — physics and technology*. Int. J. Electr. Eng. Educ. (1986). https://doi.org/10.1177/002072098602300117
64. P. Singh, N.M. Ravindra, Temperature dependence of solar cell performance—an analysis. Sol. Energy Mater. Sol. Cells. **101**, 36–45 (2012). https://doi.org/10.1016/j.solmat.2012.02.019
65. J. Li et al., 10% efficiency Cu2ZnSn(S,Se)4 thin film solar cells fabricated by magnetron sputtering with enlarged depletion region width. Sol. Energy Mater. Sol. Cells **149**, 242–249 (2016). https://doi.org/10.1016/j.solmat.2016.02.002
66. M. Ayad, M. Fathi, A. Mellit, Study and performance analysis of perovskite solar cell structure based on organic and inorganic thin films. Optik **233**, 166619 (2021). https://doi.org/10.1016/j.ijleo.2021.166619
67. Design and simulation of high efficiency tin halide perovskite solar cell. Int. J. Renew. Energy Res. no v7i4. (2017). https://doi.org/10.20508/ijrer.v7i4.6182.g7270
68. Sadanand, P.K. Singh, S. Rai, P. Lohia, D.K. Dwivedi, Comparative study of the CZTS, CuSbS2 and CuSbSe2 solar photovoltaic cell with an earth-abundant non-toxic buffer layer. Sol. Energy **222**, 175–185 (2021). https://doi.org/10.1016/j.solener.2021.05.013
69. A. Maoucha, T. Berghout, F. Djeffal, H. Ferhati, Machine learning-assisted investigation of CIGS thin-film solar cell degradation using deep learning analysis. J. Phys. Chem. Solids **199**, 112526 (2025). https://doi.org/10.1016/j.jpcs.2024.112526
70. A. Maoucha, T. Berghout, F. Djeffal, H. Ferhati, Machine learning-assisted analysis of lead-free FACsSnI3 solar cell degradation: deep learning classification and design parameter importance assessment. Inorg. Chem. Commun. **174**, 114114 (2025). https://doi.org/10.1016/j.inoche.2025.114114
71. A. Maoucha, T. Berghout, F. Djeffal, H. Ferhati, Machine learning-guided analysis of CIGS solar cell efficiency: deep learning classification and feature importance evaluation. Sol. Energy **287**, 113251 (2025). https://doi.org/10.1016/j.solener.2025.113251
72. N. Shrivastav et al., Advanced computational techniques for optimizing manganese-based perovskite solar cells: from SCAPS-1D simulations to machine learning predictions. J. Electron. Mater. **54**(2), 1209–1217 (2025). https://doi.org/10.1007/s11664-024-11638-0